remote sensing

MDPI

Article

Estimating Leaf Area Index in Apple Orchard by UAV Multispectral Images with Spectral and Texture Information

Junru Yu [1], Yu Zhang [1], Zhenghua Song [1], Danyao Jiang [1], Yiming Guo [1], Yanfu Liu [1] and Qingrui Chang [1,2,*]

[1] College of Natural Resources and Environment, Northwest A&F University, Xianyang 712100, China; yujunru@nwafu.edu.cn (J.Y.); yzhhang@nwsuaf.edu.cn (Y.Z.); songzh@nwafu.edu.cn (Z.S.); jiangdy@nwsuaf.edu.cn (D.J.); guoym@nwafu.edu.cn (Y.G.); hexogen@nwsuaf.edu.cn (Y.L.)

[2] Key Laboratory of Plant Nutrition and Agri-Environment in Northwest China, Ministry of Agriculture, Xianyang 712100, China

* Correspondence: changqr@nwafu.edu.cn; Tel.: +86-1357-183-5969

Abstract: The Leaf Area Index (LAI) strongly influences vegetation evapotranspiration and photosynthesis rates. Timely and accurately estimating the LAI is crucial for monitoring vegetation growth. The unmanned aerial vehicle (UAV) multispectral digital camera platform has been proven to be an effective tool for this purpose. Currently, most remote sensing estimations of LAIs focus on cereal crops, with limited research on economic crops such as apples. In this study, a method for estimating the LAI of an apple orchard by extracting spectral and texture information from UAV multispectral images was proposed. Specifically, field measurements were conducted to collect LAI data for 108 sample points during the final flowering (FF), fruit setting (FS), and fruit expansion (FE) stages of apple growth in 2023. Concurrently, UAV multispectral images were obtained to extract spectral and texture information (Gabor transform). The Support Vector Regression Recursive Feature Elimination (SVR-REF) was employed to select optimal features as inputs for constructing models to estimate the LAI. Finally, the optimal model was used for LAI mapping. The results indicate that integrating spectral and texture information effectively enhances the accuracy of LAI estimation, with the relative prediction deviation (RPD) for all models being greater than 2. The Categorical Boosting (CatBoost) model established for FF exhibits the highest accuracy, with a validation set R^2, root mean square error (RMSE), and RPD of 0.867, 0.203, and 2.482, respectively. UAV multispectral imagery proves to be valuable in estimating apple orchard LAIs, offering real-time monitoring of apple growth and providing a scientific basis for orchard management.

Keywords: LAI; UAV multispectral images; gabor transform; apple orchard; CatBoost

Citation: Yu, J.; Zhang, Y.; Song, Z.; Jiang, D.; Guo, Y.; Liu, Y.; Chang, Q. Estimating Leaf Area Index in Apple Orchard by UAV Multispectral Images with Spectral and Texture Information. *Remote Sens.* **2024**, *16*, 3237. https://doi.org/10.3390/rs16173237

Academic Editor: Mobushir Riaz Khan

Received: 1 August 2024
Revised: 28 August 2024
Accepted: 30 August 2024
Published: 31 August 2024

1. Introduction

Chinese apple (*Malus pumila* Mill.) production contributes to over half of the world's total apple output, with the Loess Plateau being one of the largest apple-producing areas globally [1,2]. The quality and quantity of apples serve as crucial indicators for assessing the agricultural economic development of the Loess Plateau [3]. The Leaf Area Index (LAI), defined as half the total leaf area per unit ground area, is an essential parameter for characterizing vegetation canopy structure and function [4,5]. Due to its relationship with vegetation evapotranspiration and photosynthesis rates, the LAI is a vital input in various models for eucalypt growth, water usage, and evapotranspiration [5–7]. It finds extensive applications in agricultural and forestry production, ecological environment monitoring, and global change research [8,9]. Accurate and timely acquisition of LAI information in apple orchards is critical for scaling physiological measurements from the leaf to the canopy level and for monitoring the health of apple trees [10].

Direct measurement of an LAI requires substantial labor and resources and damages crop leaves during field sampling, making it impractical for large-scale applications [11]. Remote sensing technology provides a rapid, efficient, and scalable method for estimating LAIs from regional to global scales [12]. Satellite remote sensing, in particular, is an effective means of large-scale agricultural monitoring because of its extensive coverage and non-destructive nature. However, satellite data often face temporal and spatial heterogeneity issues owing to the effects of clouds and cloud shadows [13]. Unmanned aerial vehicles (UAVs) have emerged as a near-ground remote sensing platform in recent years. UAVs are small, user-friendly, and can be equipped with various sensors (visible, multispectral, hyperspectral, or radar) for near-ground remote sensing, offering great potential for monitoring various crop parameters [14]. Multispectral sensors extend beyond the visible spectrum to include the red edge (RE) and near-infrared (NIR) bands, capturing more LAI information from crop canopies [15]. The pigments in green plant leaves do not absorb light above 700 nm, leading to a rapid change in reflectance in the RE region and high reflectance in the NIR region, making them more sensitive to plant LAIs [16,17]. The methods for estimating the LAI from remote sensing multispectral data generally fall into the two following categories: empirical statistical methods and physical models. Physical models are typically based on the radiative transfer model theory, such as the PROSAIL model [18], which can provide more physical information about an LAI. Nevertheless, the parameterization and computational complexity of these models are significantly increased [19]. In terms of empirical methods, researchers have established regression models based on the statistical relationship between ground-measured LAI data and remote sensing data [20]. However, statistical regression models struggle to handle interactions and nonlinear relationships between variables [21]. The introduction of machine learning has brought about new opportunities for LAI remote sensing estimation. Machine learning models learn the mapping relationship between remote sensing data and LAI, demonstrating high estimation accuracy. Algorithms such as Support Vector Machines (SVMs) [22], Random Forests (RFs) [23], and Gradient Boosting Decision Trees (GBDTs) [24] have been widely used to identify complex nonlinear relationships in remote sensing data for LAI estimation. Li et al. [25] validated the strong capability of the RF method in predicting grassland LAIs, suggesting it as an alternative to traditional empirical regression models. SVR effectively handles high-dimensional data and nonlinear problems, making it widely applicable in classification and regression tasks [26,27]. Zhang et al. [28] used three machine learning methods to predict leaf chlorophyll content in apple orchards, finding that the Categorical Boosting (CatBoost) model performed best due to its excellent generalization ability and robustness.

However, most studies estimating orchard LAI use VIs, and few have combined UAV multispectral images with texture features (TFs) and texture indices (TIs) to estimate apple orchard LAIs. Liu et al. [29] selected five vegetation indices (VIs) highly correlated with apple LAIs based on UAV multispectral data and conducted experiments on three different types of apples in Shaanxi Province. The results from the constructed LAI estimation model showed that the Gradient Boosting Decision Tree (GBDT) provided the best accuracy, with an R^2 of 0.846. Zhang et al. [30] constructed a hybrid inversion model to estimate the LAI of individual apple tree canopies by removing canopy shadows and combining the PROSAIL model with UAV multispectral image spectral indices. The results showed an R^2 of 0.74 for LAI estimation. The TFs of remote sensing images represent the spatial heterogeneity of spectral reflectance in different bands, reflecting the visual characteristics of homogeneity in the image [26,31]. These features are widely used in image recognition and classification [32,33]. Texture information enhances the identification of vegetation spatial structures and improves monitoring of vegetation growth [34,35]. Numerous studies have demonstrated that adding texture information can improve LAI estimation accuracy. Qiao et al. [26] developed a model to estimate peanut LAIs based on spectral and texture information extracted from UAV multispectral images. Using spectral and texture information (Grey Level Co-occurrence

Matrix, GLCM) from UAV multispectral images, Li et al. [36] estimated the LAI of winter wheat at two critical growth stages. The results both indicated that the LAI estimation models incorporating VIs and TFs were more accurate than those using a single type of information. The Gabor transform, also known as the windowed Fourier transform (with the Gaussian function as the window function), is a conversion from the time domain to the frequency domain. It has excellent properties for extracting local spatial and frequency domain information, addressing the limitations of the Fourier transform in describing local frequency domain features. The Gabor transform identifies specific directional patterns in images and analyzes them at various scales, thus providing rich feature information [37–40]. Currently, most quantitative inversion studies use GLCM for TF extraction, with limited use of the Gabor transform. The suitability of the Gabor transform for extracting texture information from multispectral images for LAI estimation remains to be explored.

Currently, most LAI remote sensing estimations focus on cereal crops such as corn [41], rice [31,42], and winter wheat [43], with limited research on economic crops [11]. Given the significant differences in canopy structures among various vegetation types, it is necessary to develop more accurate LAI estimation methods for apple orchards by incorporating texture information from UAV multispectral images, which can subsequently be used to monitor tree health. Therefore, a method for estimating apple orchards' LAIs based on spectral and texture information extracted from UAV multispectral images was proposed in this study. The specific research steps are as follows: (1) Extract spectral and texture features (Gabor transform) from UAV multispectral images of apple orchards at different growth stages and construct VIs and Tis. (2) Apply feature selection methods (Support Vector Regression Recursive Feature Elimination, SVR-RFE) to rank the importance of VIs, TFs, and TIs and filter out the most critical features. (3) Construct the SVR, RFR, and Catboost models to estimate LAIs using VIs and TFs, or VIs, TFs, and TIs as inputs, respectively, to explore the optimal estimation model. (4) The optimal model was then employed to map the orchard's LAI. The results demonstrate that combining VIs with texture information significantly improves the accuracy of LAI estimation for apple canopies, with the Catboost model achieving the highest precision. This approach offers a valuable tool for precision agriculture in apple orchards and provides important insights for future vegetation parameter estimation based on UAV imagery.

2. Materials and Methods

2.1. Study Area

The study area is located in Wuquan Town, Yangling District, Xianyang City, Shaanxi Province (108°0′57″, 34°18′47″), covering an area of about 3.75 hectares (Figure 1a). Yangling is situated within a river valley plain in the Fenwei Valley agricultural area of the Loess Plateau. The climate type is characterized by a continental monsoon semi-humid climate, with an average annual temperature of 12.9 °C and an average annual precipitation of 635.1–663.9 mm [11]. It exhibits distinct day–night temperature differences and four distinct seasons, which are conducive to the growth of apple trees, facilitating fruit sugar accumulation and improving fruit quality and taste. Additionally, the soil type in Yangling is Lou soil, known for its good permeability and fertility, which promotes the development of apple tree roots (https://www.ylq.gov.cn/zjyl/ylgl/93.htm, accessed on 1 May 2024). The orchard has been cultivating apples for 11 years and represents a typical apple orchard.

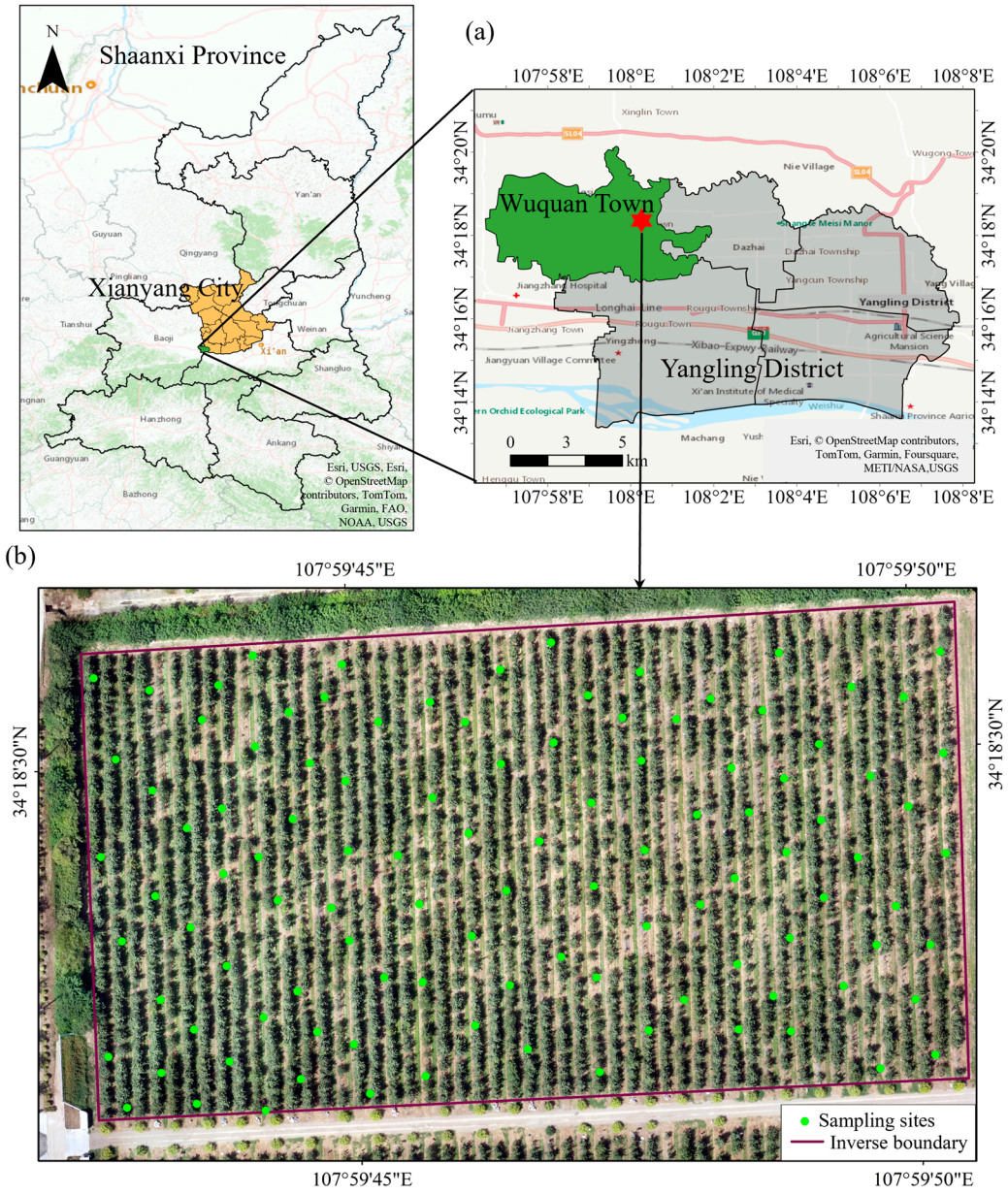

Figure 1. (**a**) Geographic location of the study area; (**b**) UAV image and sampling sites. The red star indicates our study area. In (**a**), the orange area denotes Xianyang City, the green area signifies Wuquan Town, and the gray area indicates Yangling District.

2.2. Data Acquisition and Processing

The growth cycle of apple trees is relatively long. Blooming occurs in mid-March, followed by fruit-bearing in May, with the harvest taking place in the autumn. Typically, an apple tree begins to produce fruit 2–3 years after planting and then follows a consistent developmental cycle, including stages such as bud breaking (BB), flowering, final flowering (FF), fruit setting (FS), fruit expansion (FE), and maturation [44,45]. The LAI increases rapidly during the FF stage and maintains a high level from the vigorous growth phase to the harvest stage, as an increased number of leaves are essential for nutrient absorption and transpiration during fruit development [6]. LAI measurements and UAV multispectral image collection in this study were conducted at the following three different growth stages of apple trees in 2023: the FF on 30 May, the FS on 3 July, and the FE on 11 August. A total of 108 apple trees were uniformly selected as sampling

points within the orchard (Figure 1b), with the coordinates of sampling points remaining consistent across all stages. The specific workflow diagram is shown in Figure 2.

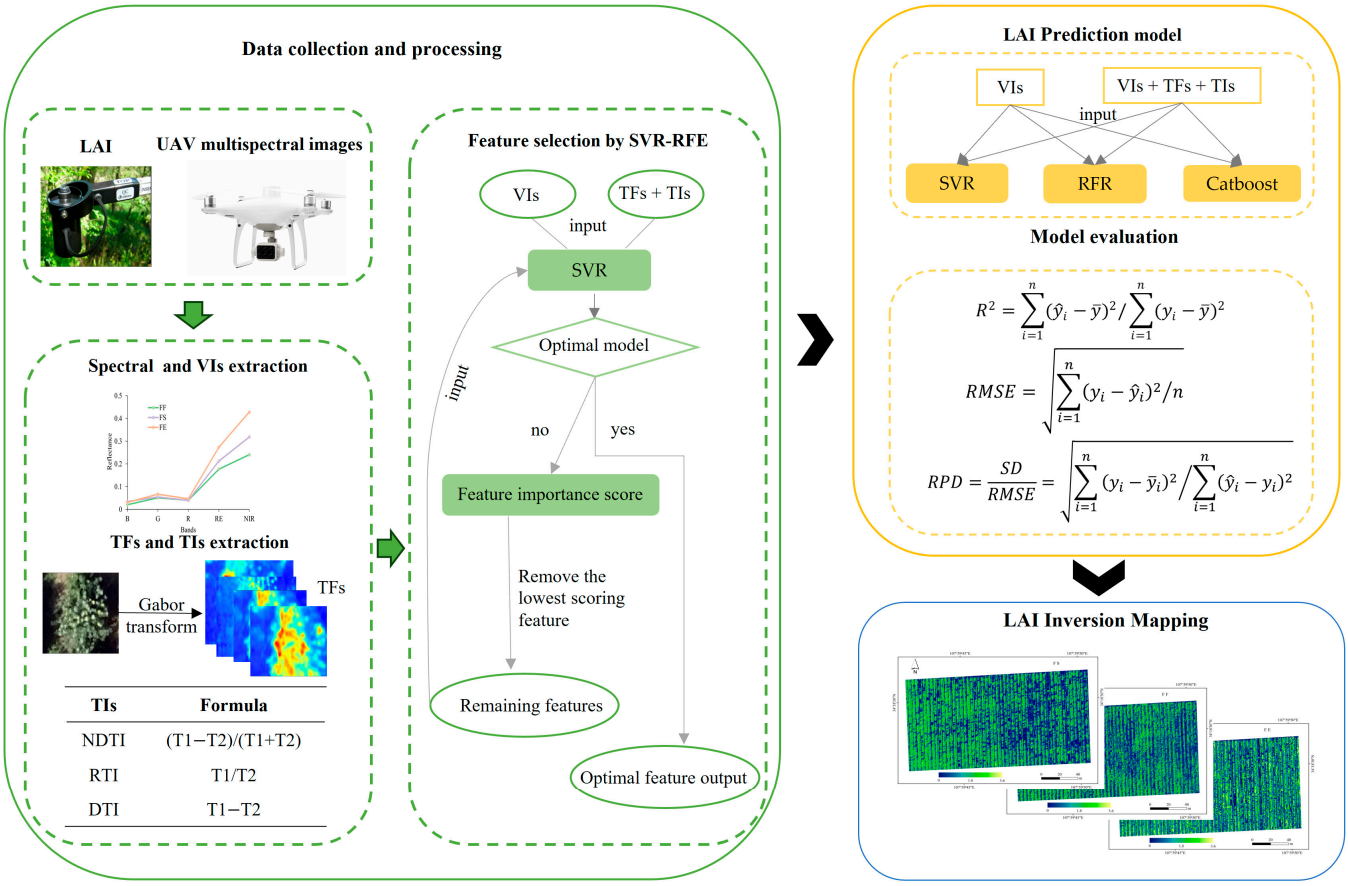

Figure 2. Flowchart of data analysis and processing.

2.2.1. LAI Measurement

An apple canopy LAI image was obtained using the CI-110 Plant Canopy Imager (CID Inc., Washington, DC, USA) and LAI calculation was undertaken using the CI-110 Plant Canopy Analysis software (https://cid-inc.com/, accessed on 11 March 2024). Leveraging its unique design features, such as a 170° fisheye lens and an 8-megapixel high-resolution camera, the CI-110 ensured clarity and coverage of image acquisition. The operating principle of the CI-110 is based on the canopy gap fraction method, which indirectly estimates the LAI by measuring the proportion of visible sky under the canopy. This method is not only efficient but also non-invasive to plants. The CI-110 was positioned about 0.5 m above the ground to ensure data reliability and accuracy during observations [11]. Each sampling point underwent two independent observations, with the average value being taken as the final LAI for that sampling point. Figure 3 illustrates the observation and processing of the apple canopy during the FS using the CI-110.

2.2.2. Acquisition and Processing of UAV Multispectral Image

DJI Phantom 4 Multispectral drone (DJI Innovations, Shenzhen, China) was utilized to acquire multispectral images of the study area (Table 1). Before acquiring the UAV data, it is essential to perform radiometric calibration to characterize the sensor's response under current environmental conditions. The flight altitude was uniformly set at 30 m, with a flight speed of 5 m/s and longitudinal and lateral overlap rates set at 75%. Flight times were selected to be in the clear, windless morning periods. The multispectral images underwent geometric correction, registration, and stitching using Pix4D Mapper software to obtain the

reflectance data. In ArcGIS 10.8 software, buffer zones were established for the sampling points, with a radius of 0.5 m yielding the best correlation between band reflectance and the LAI [11]. Subsequently, the average reflectance value of all raster cells within each buffer zone was calculated and assigned as the reflectance value for the respective sampling point. This process produced reflectance data for 108 sampling points at each growth stage.

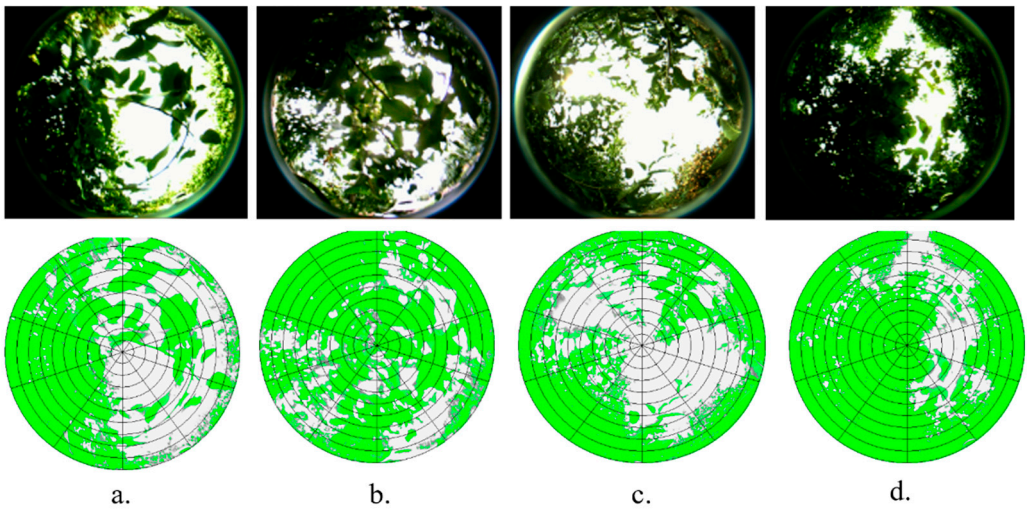

Figure 3. Partial images taken by CI-110 and processing results at the FS on July 3rd. The longitudes and latitude are (**a**) 107°59′49″E, 34°18′28″N; (**b**) 107°59′48″E, 34°18′30″N; (**c**) 107°59′47″E, 34°18′29″N; and (**d**) 107°59′45″E, 34°18′31″N.

Table 1. Detailed parameters information of multispectral UAV used in this study.

UAV Parameter		Value
Central wavelength	Blue (B)	450 nm
	Green (G)	560 nm
	Red (R)	650 nm
	Red-edge (RE)	730 nm
	Near-infrared (NIR)	840 nm
Maximum flight speeds	Ascending	6 m/s
	Descending	3 m/s
	Horizontal flight	50 km/h
Weight	Total weight	1.487 kg
Ground Sampling Distance	(flight altitude/18.9) cm/pixel	1.59 cm/pixel

2.3. Methods

2.3.1. Construction of Vegetation Indices, Texture Features, and Texture Indices

Vegetation indices, obtained through mathematical calculations on particular spectral bands, effectively mitigate the impact of sensor and environmental noise on targets. Moreover, combinations of reflectance from different bands can partially mitigate the influence of leaf physical properties (leaf structure, orientation, and radiation angle) on canopy spectra. For example, the Normalized Difference Vegetation Index (NDVI) is derived by applying a nonlinear stretch to the reflectance of NIR and R bands, thereby enhancing the contrast between them. It is commonly employed to monitor vegetation growth and mitigate certain radiometric errors. NDVI values range from −1 to 1, with positive values indicating the presence of vegetation [46]. The Ratio Vegetation Index (RVI), defined as the ratio of NIR to R reflectance, is highly sensitive to vegetation. In areas with healthy green vegetation, the RVI is significantly greater than 1, whereas, for bare surfaces, it typically hovers around 1 [47]. Due to the limited research on the LAI of apple orchards, we referenced previous studies estimating the LAIs of apple orchards, kiwi orchards, maize,

and winter wheat [10,28,30,39,43]. In this study, 19 VIs were calculated from the B, G, R, RE, and NIR bands for the inversion of the apple canopy LAI, as detailed in Table 2.

Table 2. Vegetation indices used in this study.

VIs	Formula	Reference
NDVI	(NIR − R)/(NIR + R)	[46]
RVI	NIR/R	[47]
Difference Vegetation Index (DVI)	NIR − R	[48]
Transformed Normalized Difference Vegetation Index (TNDVI)	$\sqrt{NDVI + 0.5}$	[49]
Renormalized Difference Vegetation Index (RDVI)	$(NIR - R)/\sqrt{NIR + R}$	[50]
Normalized Green–Red Difference Index (NGRDI)	(G − R)/(G + R)	[51]
Normalized Green Index (NGI)	G/(NIR + R + G)	[52]
Normalized Difference Red Edge Index (NDRE)	(NIR − RE)/(NIR + RE)	[53]
Enhanced Vegetation Index (EVI)	2.5[(NIR − R)/(NIR + 6R − 7.5B + 1)]	[54]
Optimized Soil Adjusted Vegetation Index (OSAVI)	(NIR − R)/(NIR − R + 0.16)	[55]
MERIS terrestrial chlorophyll index (MTCI)	(NIR − RE)/(RE − R)	[56]
Chlorophyll Index Red Edge (CIRE)	NIR/RE − 1	[57]
2-Band Enhanced Vegetation Index (EVI2)	2.5(NIR − R)/(1 + NIR + 2.4R)	[58]
Green Normalized Difference Vegetation Index (GNDVI)	(NIR − G)/(NIR + G)	[59]
Triangle Vegetation Index (TVI)	60(NIR − G) − 100(R − G)	[60]
Visible Atmospherically Resistant Index (VARI)	(G − R)/(G + R − B)	[61]
Soil Adjusted Vegetation Index (SAVI)	1.5(NIR − R)/(NIR + R + 0.5)	[62]
Modified Triangle Vegetation Index (MTVI)	1.2[1.2(NIR − G) − 2.5(R − G)]	[63]
Structure Insensitive Pigment Index (SIPI)	(NIR − B)/(NIR − R)	[64]

Gabor transform involves filtering images using Gabor filtering, where the phase parameter controls the return value of the Gabor function, comprising both real and imaginary parts. The imaginary part represents the odd-symmetric filter, while the real part represents the even-symmetric filter. The texture features of the image are derived from the modulus of the real and imaginary parts (Formulas (1)–(5)) [40,65].

Real:

$$g(x,y) = e^{\left(-\frac{x'^2+\gamma^2y'^2}{2\sigma^2}\right)}cos\left(2\pi\frac{x'}{\lambda} + \varnothing\right) \quad (1)$$

Imaginary:

$$g(x,y) = e^{\left(-\frac{x'^2+\gamma^2y'^2}{2\sigma^2}\right)}sin\left(2\pi\frac{x'}{\lambda} + \varnothing\right) \quad (2)$$

$$x' = xcos(\theta) + ysin(\theta) \quad (3)$$

$$y' = ycos(\theta) - xsin(\theta) \quad (4)$$

$$T = \sqrt{real^2 + imaginary^2} \quad (5)$$

where x and y denote the pixel coordinates in the image while x' and y' represent the new position coordinates generated by the rotated Gabor kernel function. λ represents the wavelength, θ signifies the orientation of the parallel stripes in the Gabor function, $\varnothing$ denotes the phase offset, σ stands for the standard deviation of the Gaussian function, and γ represents the spatial aspect ratio. *real* and *imaginary*, respectively, denote the real and imaginary parts.

In apple canopy LAI research, Gabor filtering was applied to process UAV multispectral images, extracting the four statistical features, mean (MEAN), variance (VAR), second moment (SEC), and correlation (CORR), across the five spectral channels [66]. Following fine-tuning, the parameters of the Gabor filtering were set to a window size of 3 × 3, a kernel size of 9, a sigma of 1, a theta of 0, a lambda of 5, a gamma of 0.5, a psi of 0, and an angle of 0, resulting in the optimal texture feature extraction. A total of 20 texture features were extracted for each period. To simplify the nomenclature of texture features, band

names were added to differentiate the texture information of each band. For instance, "MEAN-R" denotes the mean value of the R.

TFs from different bands were combined to construct the TIs [67], including a Normalized Difference Texture Index (NDTI), a Ratio Texture Index (RTI), and a Difference Texture Index (DTI) (Table 3). A total of 570 TIs were extracted for each period. To simplify the nomenclature of TIs, texture features and band names were added in the LAI research to differentiate each TI composed of texture information from different bands. For example, "$NDTI_{MEAN\text{-}R/SEC\text{-}RE}$" represents the NDTI formed by the MEAN of R and SEC of RE.

Table 3. Texture indexes constructed in this study.

TIs	Formula
Normalized Difference Texture Index (NDTI)	$(T1 - T2)/(T1 + T2)$
Ratio Texture Index (RTI)	$T1/T2$
Difference Texture Index (DTI)	$T1 - T2$

where T1 and T2 represent two different selected texture features.

2.3.2. Feature Importance Ranking

Support Vector Regression-Recursive Feature Elimination (SVR-RFE) is a feature selection method based on SVR that is designed to eliminate redundant information among features. It utilizes the model coefficients of SVR to assess feature importance and employs a recursive feature elimination strategy to select variables. The main process of using this method for sorting and filtering features in this study includes the following: (1) Features are initially input into the SVR model for training to determine if the model is optimal. (2) If the model is optimal, the best features are output. Otherwise, the importance score of each feature is calculated, and the least important feature is removed. (3) The remaining features are then re-input into the SVR model for further training until the optimal model is achieved. (4) The features are ranked according to their importance based on the removal sequence [68]. During feature selection, the dataset was split into training and testing sets in a 7:3 ratio, with the random seed set to 42 to ensure reproducibility. The Radial Basis Function (RBF) kernel was used with other parameters set to default. Cross-validation was employed to select the optimal features.

In this study, VIs were initially used as inputs for feature importance ranking to select the optimal VIs for constructing the LAI estimation model. Subsequently, all TFs and TIs were input into the SVR-RFE to identify the best combination of TFs and TIs. The selected VIs, TFs, and TIs were then used as inputs to build the model, aiming to investigate whether incorporating texture information improves the accuracy of the LAI estimation.

2.3.3. Modeling Methods

CatBoost is an open-sourced machine learning algorithm created by the Russian search engine company Yandex in 2017. It optimizes the GBDT algorithm and integrates multiple base learners using a serial method. There are dependencies among the base learners generated during training. The final result is obtained by weighting the regression values of all base learners [69]. CatBoost uses a greedy strategy to build models, allowing them to gradually learn the underlying patterns and structure of the data, thereby effectively improving prediction accuracy. By applying Ordered Boosting to address the gradient bias issues, CatBoost considers the importance of features and sequentially adds them according to their importance. Additionally, it employs Oblivious Trees as base predictors, endowing the model with stronger robustness and generalization capabilities. CatBoost has the following four important parameters: iterations (maximum number of decision trees), learning rate (controls the convergence speed of the model), depth (maximum depth of the trees), and loss function. CatBoost was employed to estimate the LAI of the apple orchard in this study. RMSE was chosen as the loss function, and a grid search with cross-validation was conducted to optimize the model's hyperparameters. The number of iterations was set within the range of 100 to 1000 with intervals of 100, while the learning rate was set

within the range of 0.01 to 0.1 with arbitrary values to mitigate overfitting. The depth was constrained to integers between 6 and 12 while other parameters in the model were kept at their default values.

RFR is an ensemble learning algorithm that utilizes Bootstrap sampling with replacement to randomly select subsets of training samples and variables, generating multiple decision trees [23]. In handling regression problems, RFR derives the final prediction by averaging the predicted values of all decision trees. It excels at handling high-dimensional and large-scale datasets and showcasing a good generalization performance [70,71]. RFR can randomly select features for branching, increasing model diversity and making the model more robust and less susceptible to noisy data and outliers. By combining the predictions of multiple relatively independent decision trees, RFR mitigates the potential overfitting issues of individual models, thus improving the overall model's generalization ability [72]. Only two parameters were defined with specified ranges in this study: n_estimators (number of trees in the forest), and max_depth (maximum depth of the trees), ranging from 80 to 150 and 3 to 5, respectively. All other parameters were set to their default values.

Support Vector Regression (SVR) is a regression analysis method based on structural risk minimization and statistical theory [22]. It demonstrates strong adaptability when dealing with regression problems with more dimensions than samples. SVR introduces kernel functions to build complex decision boundaries in high-dimensional space, effectively handling nonlinear regression problems. Additionally, the algorithm controls model complexity by introducing a penalty coefficient (C) to prevent overfitting. The RBF kernel function with a gamma value of 0.1 was employed for SVR calculations in this study. Model parameters were optimized using cross-validation and grid search methods to enhance the model's generalization ability. The C values were set between 5 and 50, while epsilon was kept at its default of 0.1; all other parameters remained at their default values.

2.3.4. Model Evaluation Indices

The model accuracy is evaluated using the coefficient of determination (R^2), root mean square error (RMSE), and relative prediction deviation (RPD) metrics. The formulas for these metrics are used to assess the model's performance. A higher R^2 closer to 1 indicates a better fit of the model to the response variable. The RMSE reflects the deviation between simulated values and actual measurements; a lower RMSE suggests that the predicted values are closer to the actual measurements, indicating better model performance. An RPD greater than 2 indicates an excellent predictive ability in the model in regard to the response variable. RPD values between 1.4 and 2 suggest that the model only has a rough predictive capability for the response variable. RPD values less than 1.4 indicate that the model lacks a predictive ability for the response variable [73].

$$R^2 = \sum_{i=1}^{n} (\hat{y}_i - \overline{y})^2 / \sum_{i=1}^{n} (y_i - \overline{y})^2 \quad (6)$$

$$RMSE = \sqrt{\sum_{i=1}^{n} (y_i - \hat{y}_i)^2 / n} \quad (7)$$

$$RPD = \frac{SD}{RMSE} = \sqrt{\sum_{i=1}^{n} (y_i - \overline{y}_i)^2 / \sum_{i=1}^{n} (\hat{y}_i - y_i)^2} \quad (8)$$

where y_i and $\hat{y}_i$ represent the measured and predicted values of the LAI and $\overline{y}_i$ denotes the mean of the observed values in the modeling or validation dataset. n is the sample size and SD is the standard deviation.

3. Results

3.1. Apple Orchard LAI and Multispectral Feature Analysis

The LAI ranges of sample points selected for the FF, FS, and FE growth stages are 0.19 to 2.21, 0.34 to 2.82, and 0.28 to 3.50, respectively (Table 4). The coefficients of variation for the three growth stages are 43.54%, 45.21%, and 39.83%, all indicating moderate variability (CV between 0.1 and 1). As the growth stages progress, the canopy structure of apple trees undergoes continuous changes, with the LAI showing a gradual increasing trend. During FE, the mean and maximum values of the LAI reach their peaks. As the apple growth stage changes, the number, area, and quality of apple leaves gradually increase. The leaf area and quantity continue to increase to achieve high fruit yield during the fruit expansion period, leading to the peak of the LAI. The samples are divided into prediction and validation sets in a 7:3 ratio, resulting in 74 prediction sets and 34 sample sets for each growth stage.

Table 4. Apple orchard LAI statistics at different growth stages.

Growth Stage	Sample Size	Min	Max	Mean	Standard Deviation (SD)	Coefficient of Variation (CV, %)
FF	108	0.19	2.21	1.19	0.52	43.54
FS	108	0.34	2.82	1.47	0.66	45.21
FE	108	0.28	3.50	1.89	0.75	39.83

Figure 4 displays the average reflectance obtained from UAV-based multispectral images across all samples during three growth stages. The spectral trends during different growth stages show the following consistent pattern: low reflectance in the B, G, and R bands, followed by a sharp increase in the RE band, and peaking in the NIR band. In the visible light region, apple leaf pigments absorb blue and red light while reflecting green light, creating a reflectance peak (G peak) and two absorption valleys (B and R valley). The reflectance in these visible light bands exhibit minimal variation across different growth stages. Conversely, in the NIR region, the cellular structure of the leaves strongly reflects electromagnetic radiation, resulting in the characteristic high reflectance associated with vegetation. As the growth stages advance, the apple tree leaves undergo more vigorous development, leading to a gradual increase in both RE and NIR reflectance. These observations are consistent with the findings reported by Zhang et al. [30].

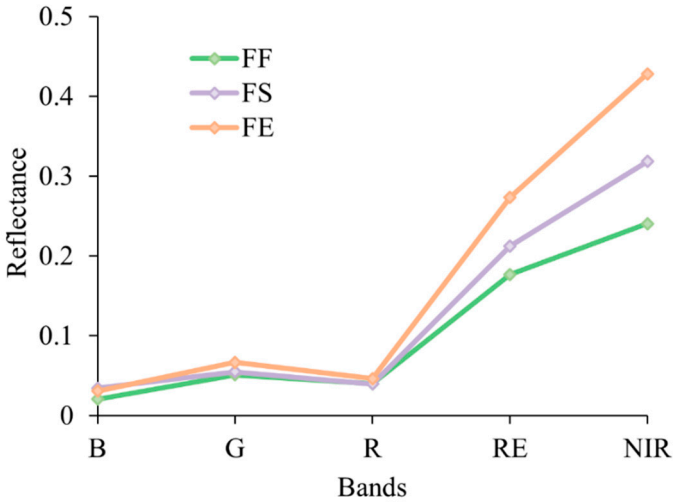

Figure 4. Multispectral characteristics of apple canopy during different growth stages.

3.2. Correlation Analysis between LAI and Both Spectral and Texture Information

The correlations between the LAI and the VIs, TFs, and TIs are shown in Tables 5 and 6 and Figure 5. Figure 5 illustrates the correlations between the DTI, which consists of any two TFs, and the LAI at three growth stages. The complete correlation heatmap is provided

in Figure A1. During the three growth stages, the DTI, NDTI, and RTI formed by the MEA and SEC of the RE and NIR bands, in combination with the TFs of other bands, exhibited a high correlation with the LAI. This further indicates that the RE and NIR bands are more sensitive to the LAI. During FF, 19 VIs and six TFs reached a highly significant level ($p < 0.01$), with correlation coefficients ranging from 0.45 to 0.81 and 0.46 to 0.78. The TIs with the highest absolute correlation coefficient for DTI, RTI and NDTI all exceeded 0.79. At FS, 21 VIs and 10 TFs reached a highly significant level, with correlation coefficients ranging from 0.44 to 0.82 and 0.44 to 0.63. The TIs with the highest absolute correlation coefficient were all exceeding 0.78. In FE, 20 VIs and 6 TFs reached a highly significant level, with correlation coefficients ranging from 0.42 to 0.81 and 0.56 to 0.77. The TIs with the highest absolute correlation coefficient were all exceeding 0.78. These results indicate that the correlation of TIs is superior to that of TFs and that the parameters with the highest correlation vary across different growth stages.

Table 5. Correlation coefficients between VIs and LAI at different growth stages.

VIs	Correlation Coefficients		
	FF	FS	FE
B	−0.14	−0.08	0.07
G	0.51 **	0.03	0.26 **
R	−0.10	−0.61 **	−0.33 *
RE	0.73 **	0.44 **	0.67 **
NIR	0.78 **	0.57 **	0.75 **
NDVI	0.55 **	0.75 **	0.72 **
RVI	0.50 **	0.80 **	0.74 **
DVI	0.79 **	0.66 **	0.79 **
TNDVI	0.55 **	0.75 **	0.72 **
RDVI	0.81 **	0.73 **	0.81 **
NRI	0.55 **	0.82 **	0.72 **
NGI	−0.51 **	−0.60 **	−0.63 **
NDREI	0.33 **	0.59 **	0.54 **
EVI	0.81 **	0.72 **	0.81 **
OSAVI	0.79 **	0.66 **	0.77 **
MTCI	0.30 **	0.28 **	0.34 **
CIRE	0.32 **	0.59 **	0.54 **
EVI2	0.80 **	0.71 **	0.81 **
GNDVI	0.50 **	0.61 **	0.63 **
TVI	0.80 **	0.68 **	0.80 **
VARI	0.56 **	0.82 **	0.72 **
SAVI	0.81 **	0.75 **	0.81 **
MTVI	0.80 **	0.69 **	0.80 **
SIPI	0.45 **	0.65 **	0.42 **

where * and ** indicate significant at the 0.05 and 0.01 levels, respectively.

Table 6. Correlation coefficients between TFs and LAI at different growth stages.

Texture Feature	Correlation Coefficient		
	FF	FS	FE
MEAN −B	0.14	−0.08	0.07
VAR −B	−0.06	0.47 **	0.35 **
SEC −B	0.06	−0.09	0.08
CORR −B	−0.03	0.49 **	0.36 **
MEAN −G	0.51 **	0.03	0.28 **
VAR −G	0.01	0.56 **	0.56 **
SEC −G	0.46 **	0.06	0.29 **
CORR −G	0.09	0.59 **	0.58 **

Table 6. *Cont.*

Texture Feature	Correlation Coefficient		
	FF	FS	FE
MEAN −R	0.10	−0.61 **	−0.32 **
VAR−R	−0.12	−0.22 *	−0.18
SEC−R	−0.01	−0.63 **	−0.36 **
CORR−R	−0.12	−0.16	−0.12
MEAN−RE	0.73 **	0.44 **	0.69 **
VAR−RE	−0.03	0.40 **	0.22 *
SEC−RE	0.69 **	0.45 **	0.69 **
CORR−RE	0.04	0.40**	0.22 *
MEAN−NIR	0.78 **	0.57 **	0.77 **
VAR−NIR	0.00	−0.14	−0.18
SEC−NIR	0.74 **	0.56 **	0.77 **
CORR−NIR	0.06	−0.08	−0.19

where * and ** indicate significant at the 0.05 and 0.01 levels, respectively.

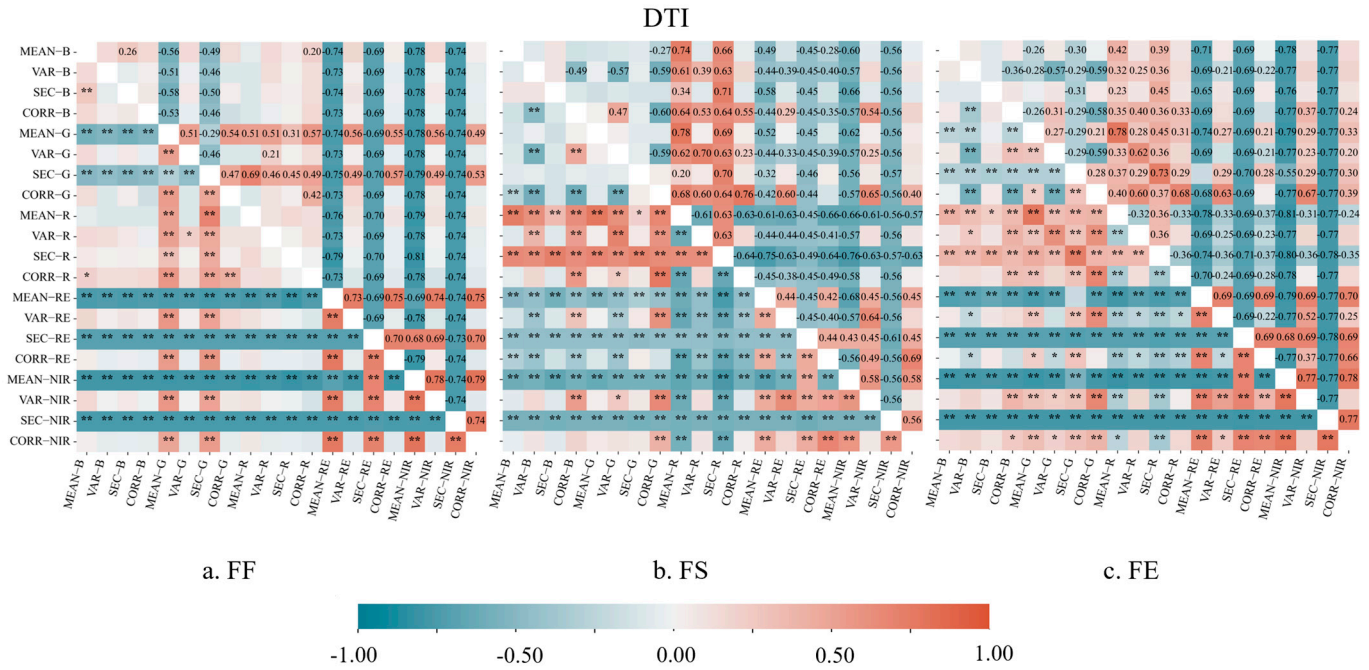

Figure 5. Correlation between DTI, composed of any two TFs, and LAI at different growth stages. * and ** indicate significant at the 0.05 and 0.01 levels, respectively.

3.3. LAI Estimation Based on VIs

The ranking of significantly correlated VIs based on SVR-RFE is depicted in Figure 6. VARI and RVI exhibit consistently good performance across all three growth stages. For FF, FS, and FE, the top 12, top 9, and top 7 ranked VIs, respectively, were selected to construct SVR, RFR, and CatBoost models for LAI estimation. The modeling and validation results are presented in Table 7, with the fitting curves on the validation set shown in Figure 7.

In FF, CatBoost demonstrated high accuracy for both modeling and validation, with a validation R^2 of 0.788 and an RPD exceeding 2.0. SVR exhibited a lower performance, with modeling and validation of the RMSE at 0.283 and 0.274, respectively. The modeling R^2 was 0.688 and the RPD was less than 2, indicating a moderate estimation capability for the LAI. RFR achieved the highest modeling R^2 of 0.868 but showed overfitting with a validation R^2 of 0.721 and an RPD of less than 2. In FS, CatBoost provided the best LAI estimation performance, with a modeling and validation R^2 of 0.799 and 0.770, respectively, and an RPD of 2.084. This was followed by SVR and RFR, with a validation R^2 of 0.707 and 0.708,

respectively. In FE, the performance of the models was ranked as CatBoost > RFR > SVR. CatBoost achieved the highest validation R^2 of 0.769 and an RPD of 2.083, along with the lowest RMSE among the three models 0.323. The scatter plot distribution generally reveals a trend where predicted values tend to be higher for lower-measured LAI values and lower for higher-measured LAI values. Overall, CatBoost exhibits the closest fit to the 1:1 line with the highest R^2 and shows the best-fitting performance.

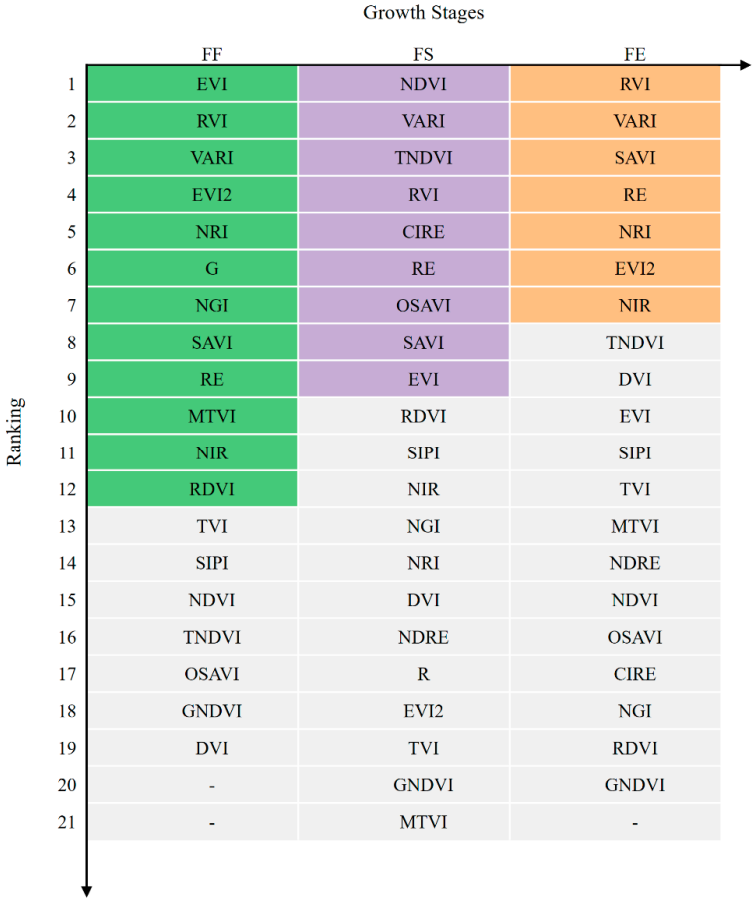

Figure 6. Feature importance ranking of VIs at different growth stages. Green indicates features preferred during the FF stage, purple represents the FS stage, and orange denotes the FE stage.

Table 7. Accuracy of LAI estimation models based on the selected VIs.

Growth Stage	Variate Size	Model	Modeling Set		Validation Set		
			R^2	RMSE	R_v^2	$RMSE_v$	RPD_v
FF	12	SVR	0.688	0.283	0.736	0.274	1.947
		RFR	0.868	0.184	0.721	0.281	1.900
		CatBoost	0.807	0.216	0.788	0.237	2.172
FS	9	SVR	0.733	0.350	0.707	0.329	1.847
		RFR	0.752	0.318	0.708	0.382	1.849
		CatBoost	0.799	0.277	0.770	0.323	2.084
FE	7	SVR	0.703	0.395	0.708	0.431	1.852
		RFR	0.782	0.358	0.716	0.374	1.875
		CatBoost	0.798	0.277	0.769	0.323	2.083

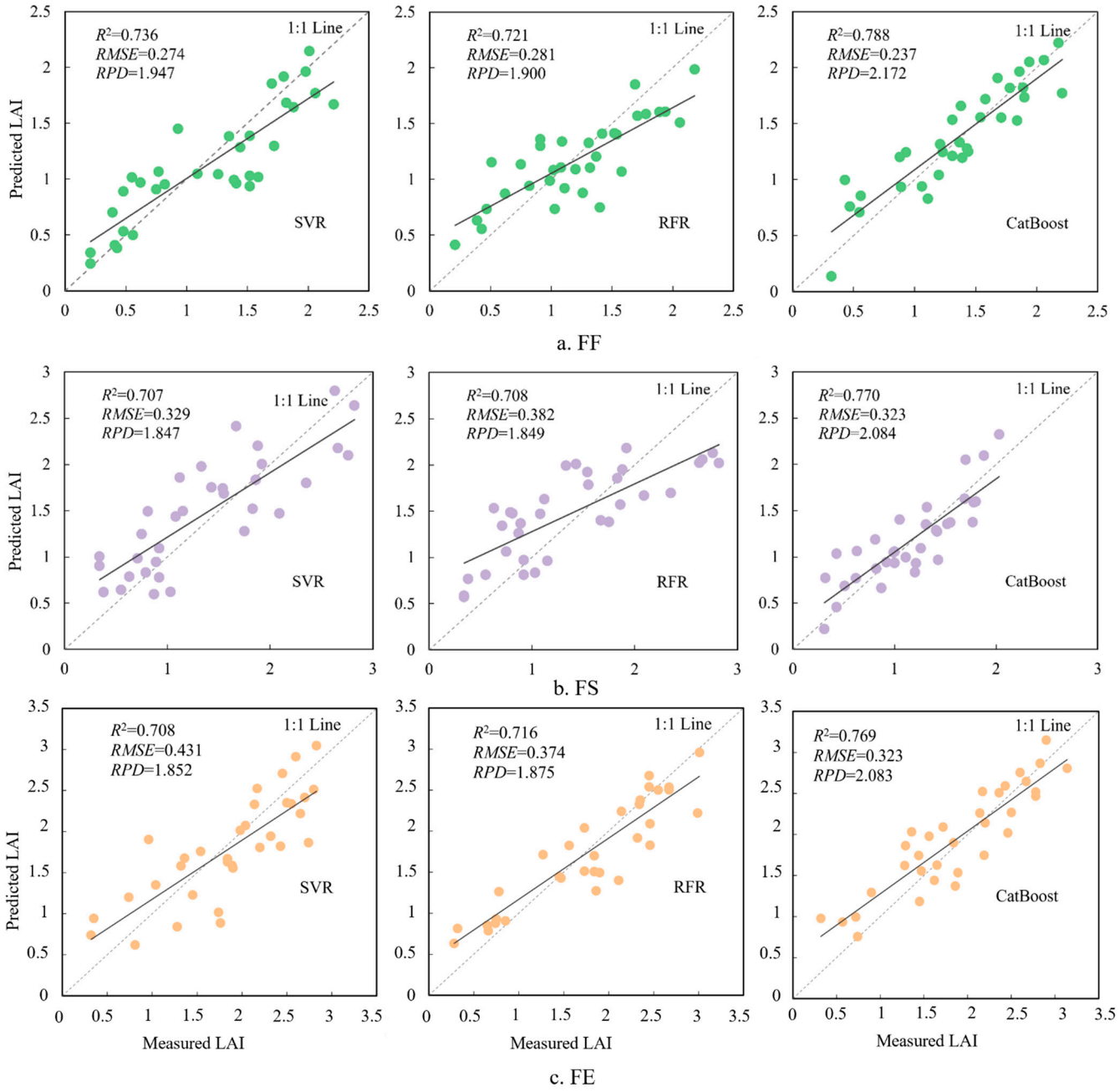

Figure 7. Validation results of SVR, RFR, and CatBoost established for LAI and VIs at different growth stages. The solid lines represent the fitted curves, and the dashed lines indicate the 1:1 line, as in subsequent figures.

3.4. LAI Estimation Based on VIs Combined with Texture Information

Through SVR-RFE, the importance rankings of TFs and TIs were determined, and the selected texture information, combined with the preferred VIs, were used as model inputs. For the FF, FS, and FE periods, the top four, top three, and top five TFs or TIs were selected, respectively. The specific TFs and TIs are shown in Table 8, with the complete rankings provided in the Supplementary Materials. The modeling and validation results are detailed in Table 9, and the fitting curves for the validation set are illustrated in Figure 8.

Table 8. The optimal combination of TFs and TIs selected by SVR-RFE.

Growth Stage	Texture Feature and Index
FF	$DTI_{SEC\text{-}R/MEAN\text{-}NIR}$ $NDTI_{CORR\text{-}R/SEC\text{-}RE}$ $RTI_{CORR\text{-}R/SEC\text{-}RE}$ MEAN-NIR
FS	$RTI_{SEC\text{-}G/SEC\text{-}R}$ $RTI_{MEAN\text{-}G/MEAN\text{-}R}$ $DTI_{SEC\text{-}R/MEAN\text{-}NIR}$
FE	$DTI_{MEAN\text{-}R/MEAN\text{-}NIR}$ $DTI_{SEC\text{-}R/MEAN\text{-}NIR}$ $RTI_{MEAN\text{-}R/SEC\text{-}RE}$ $NDTI_{MEAN\text{-}R/SEC\text{-}RE}$ MEAN-NIR

Table 9. LAI estimation model accuracy based on VIs combined with texture information.

Growth Stage	Variates Size	Model	Modeling Set		Validation Set		
			R^2	RMSE	R_v^2	$RMSE_v$	RPD_v
FF	16	SVR	0.859	0.248	0.795	0.253	2.123
		RFR	0.877	0.195	0.755	0.264	2.018
		CatBoost	0.941	0.190	0.867	0.203	2.482
FS	12	SVR	0.840	0.252	0.811	0.313	2.314
		RFR	0.868	0.244	0.787	0.286	2.165
		CatBoost	0.899	0.227	0.858	0.273	2.411
FE	12	SVR	0.815	0.303	0.797	0.373	2.263
		RFR	0.935	0.180	0.815	0.356	2.378
		CatBoost	0.913	0.200	0.840	0.280	2.386

Compared to using only VIs, incorporating texture information improved the overall accuracy of the models across all three periods, with all RPD exceeding 2. In FF, the modeling R^2 for SVR increased from 0.688 to 0.859, and the RPD rose to 2.123. RFR also showed high modeling and validation accuracy, with a validation set R^2 of 0.755, though overfitting was still observed. CatBoost provided the best LAI estimation, with an R^2 of 0.941 and 0.867 for the modeling and validation sets, respectively, and an RPD of 2.472. The R^2 for the modeling set increased by 0.134. In FS, the LAI estimation accuracy improved for all three models, with each demonstrating good estimation capability. The modeling R^2 for all models exceeded 0.84. The RPD for SVR increased from 1.847 to 2.314, an improvement of 0.467. During FE, RFR achieved the highest modeling R^2 of 0.935, but its validation R^2 was only 0.815. In contrast, CatBoost proved to be more stable, showing no signs of overfitting, with a modeling and validation R^2 of 0.913 and 0.840, respectively. The R^2 for the modeling set increased by 0.124. The inclusion of texture information increased the RPD by 0.303, reaching 2.386. Overall, CatBoost demonstrated good predictive ability across all three growth stages. The scatter plot distribution trends were consistent with the modeling results based on VIs, showing that predicted values tended to be higher for lower-measured LAI values and lower for higher-measured LAI values. Overall, the fitting curves of the CatBoost models in all three growth stages were closer to the 1:1 line, indicating the best-fitting performance.

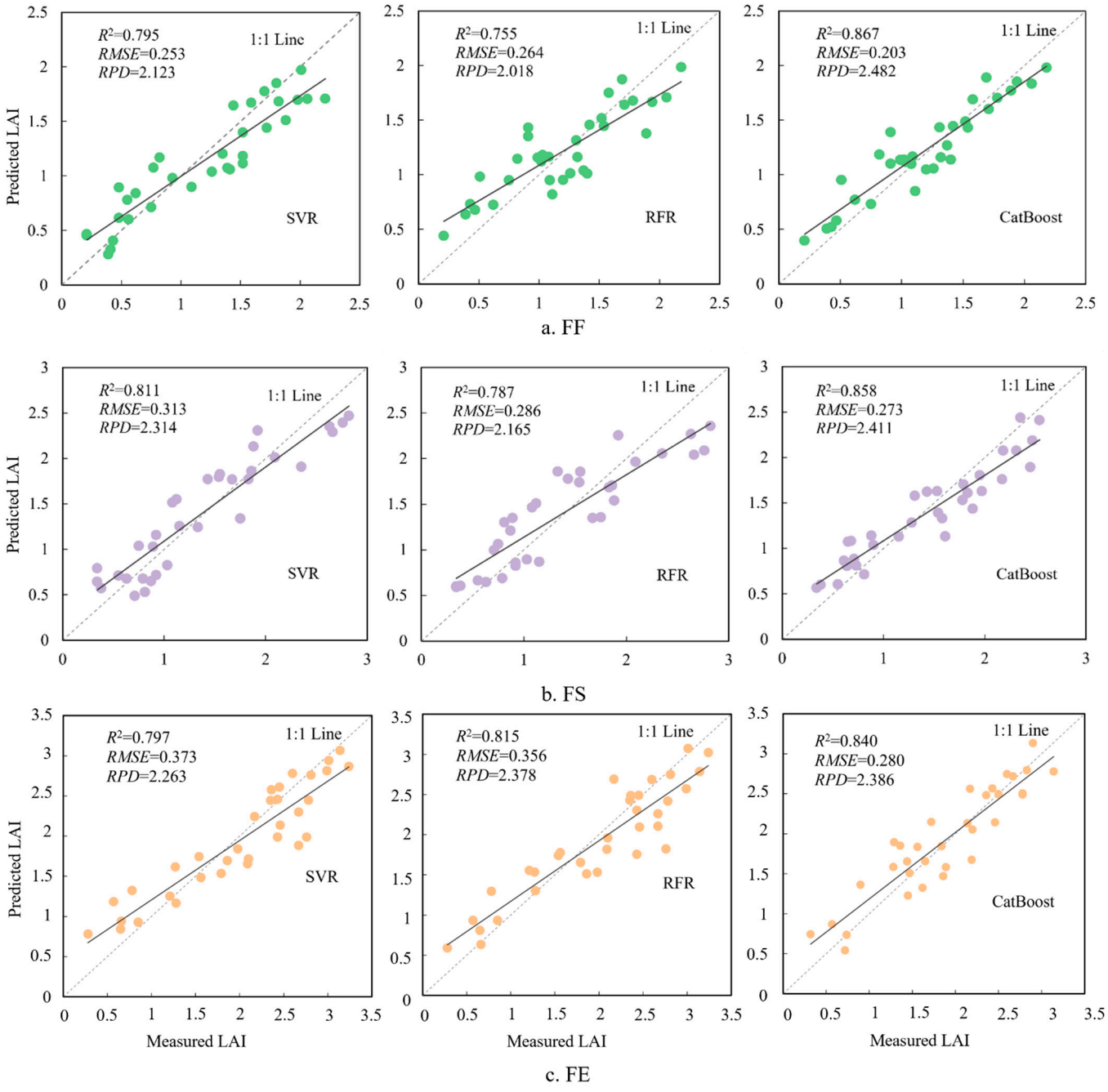

Figure 8. Validation results of SVR, RFR, and CatBoost established for LAI and VI combined texture information at different growth stages.

3.5. LAI Inversion Mapping

According to model accuracy, CatBoost with VIs combined with texture information was more suitable for the LAI estimation model for each growth stage. By incorporating the image matrix in Python, the spatial distribution mapping of the apple orchard LAI for each growth stage in the study area was conducted (Figure 9).

At FF, apple trees have ceased flowering, resulting in fewer and smaller leaves. At this point, the average LAI in the orchard is approximately 2.0. The LAI distribution exhibits a pattern of lower values in the east and higher values in the west, a trend also observed during FS. In FS, the apple trees are in a period of rapid leaf growth, with overlapping and dense leaf coverage, leading to an average LAI of around 2.5. The LAI values in the western part of the orchard mostly range from 1.8 to 2.8, while those in the eastern part range

from 0.2 to 1.8. According to the investigation, the orchard received uniform fertilization and irrigation early in the season. The differences in the LAI that were observed between the eastern and western parts of the orchard may be due to variations in the soil nutrient conditions. The soil in the eastern part of the orchard had lower nutrient levels compared to the western part, leading to slower growth and development of the trees in the east. By the late FS stage, additional fertilization was applied to the eastern part of the orchard, which accelerated tree growth due to improved nutrient availability. Thus, in FE, although the trees primarily directed nutrients to fruit development, leaf growth continued rapidly. The average LAI in the orchard reached approximately 2.8, with most values ranging from 1.2 to 3.2. This inversion map closely aligns with the actual growth conditions observed.

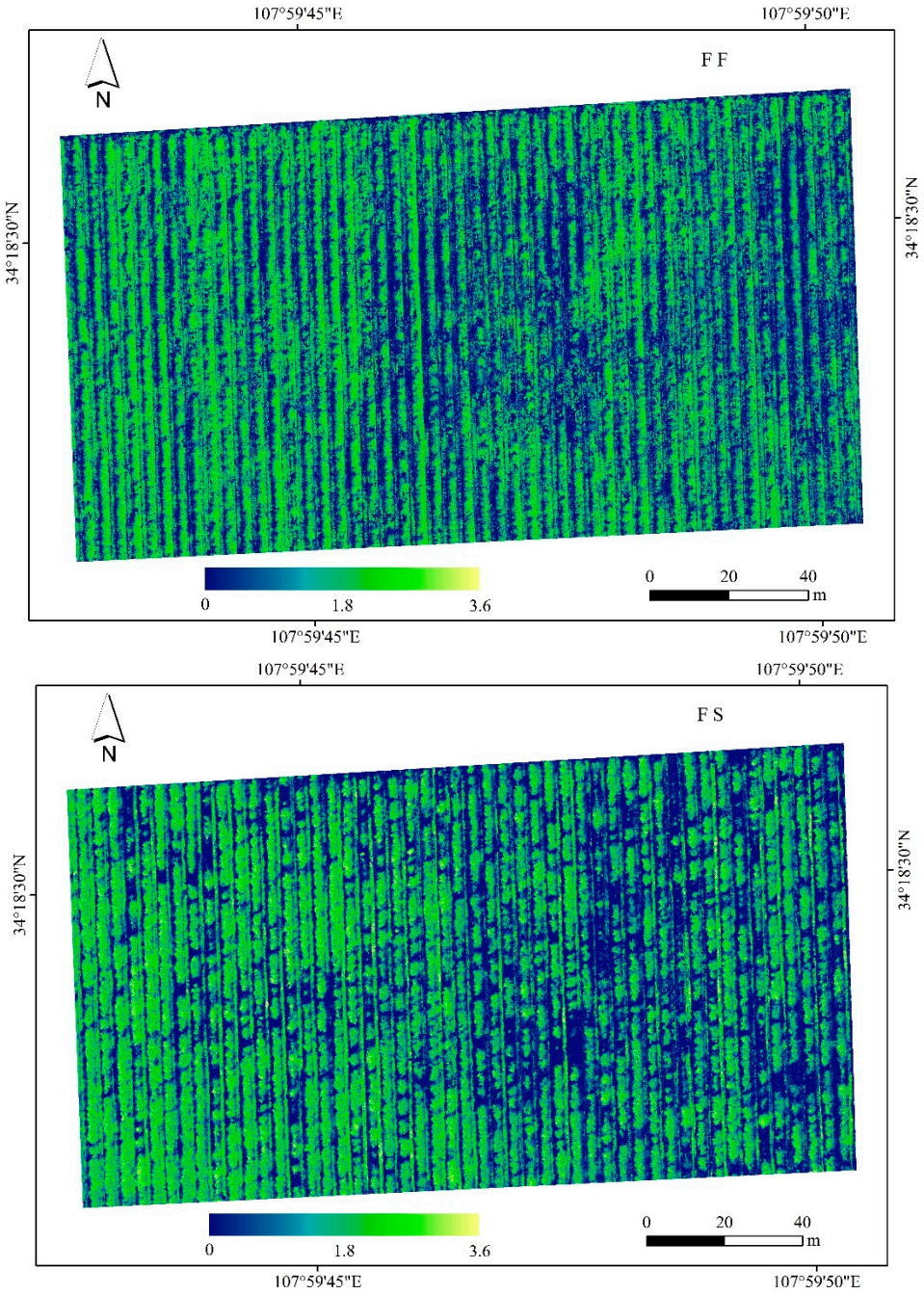

Figure 9. *Cont.*

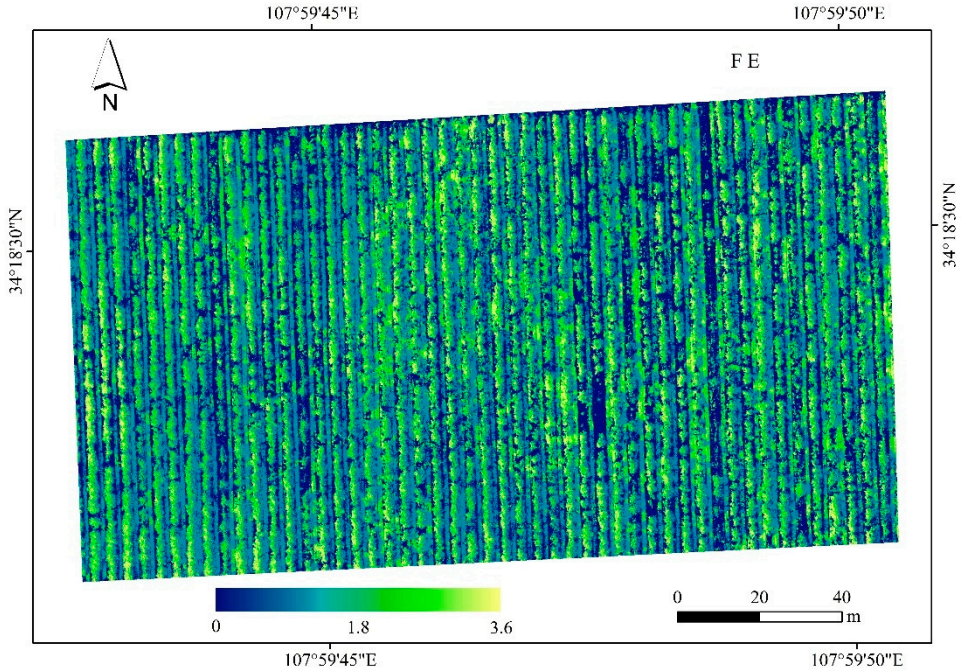

Figure 9. Spatial distribution maps of apple orchard LAI at three growth stages in this study.

4. Discussion

4.1. Feasibility of Estimating LAI with Multispectral UAV Images in Apple Orchard

Vegetation canopy reflectance in the visible light spectrum is typically influenced by pigment deposition, while the RE and NIR bands have greater penetration ability. Consequently, the RE and NIR bands are frequently employed in constructing VIs for canopy parameter research. Analysis of UAV multispectral imagery and LAI observations in apple orchards indicates that VIs derived from the R, RE, and NIR bands exhibit a higher correlation with the orchard LAI, such as SAVI, VARI, and RVI, with correlation coefficients exceeding 0.8, reaching a highly significant level ($p < 0.01$). Sun et al. [74] found that RVI had the strongest correlation with the maize canopy LAI, while Qiao et al. [10] reported a strong correlation between SAVI and the maize LAI. The correlation between individual TFs and the apple LAI is relatively weak. However, the correlation improves when TIs derived from these features are used, which is consistent with previous research findings [74–76]. Among TIs, MEAN-RE, MEAN-NIR, SEC-RE, and SEC-NIR showed a high correlation with the LAI. Zhang et al. [77] indicated that MEAN features in the R, RE, and NIR bands had strong correlations with the wheat canopy LAI; TIs calculated from NIR and RE bands had even higher correlations with the winter wheat canopy LAI. Compared to RGB UAVs, multispectral UAVs, which include visible light and RE and NIR bands sensitive to vegetation canopy structure, improve LAI estimation accuracy. Additionally, they are more maneuverable and easier to operate in real-world environments than hyperspectral UAVs, making them an ideal platform for agricultural orchard management.

4.2. Advantages of Combining Spectral and Texture Information for Estimating LAI

Texture feature provides information about the vegetation structure and details within the image, which are related to plant growth [42]. Integrating spectral and texture features enables a more comprehensive interpretation and monitoring of apple growth in a two-dimensional space, thereby enhancing model accuracy. Among the added TIs, those formed by any combination of MEAN and SEC with RE and NIR bands exhibit better correlation and are the most frequently used in modeling. MEAN and SEC primarily reflect characteristics such as image roughness, smoothness, and texture coarseness. Moreover, when texture information was input into SVR-RFE for importance ranking, TIs generally ranked higher than TFs. TIs derived from the statistical combination of two TFs help

to reduce or mitigate random noise inherent in single feature extraction, capturing the combined effects of two different texture features on the LAI [75]. The results of this study indicate that model accuracy improved across all three growth stages after incorporating TFs and TIs, with RPD exceeding 2, consistent with findings from Zhang et al. [11], Sun et al. [74] and Fei et al. [78]. In FF, the R^2 of the SVR modeling set increased the most, from 0.688 to 0.859, and the RPD rose to 2.123. The R^2 of CatBoost for the modeling set increased by 0.134. In FS, all three models demonstrated effective LAI estimation, with the modeling set R^2 exceeding 0.84. Notably, the RPD for SVR increased by 0.467. In FE, the R^2 of the RFR modeling set increased by 0.153, reaching 0.935.

4.3. Advantages of CatBoost in Estimation LAI

In this study, models constructed using VIs, TFs, and TIs selected by SVR-RFE effectively estimated LAI, with CatBoost demonstrating superior performance (Figure 10a). Although the RFR model exhibited high R^2 for certain growth stages in this study, overfitting was observed. The overall accuracy was limited, which may be due to multicollinearity among the selected features [28]. CatBoost employs a greedy strategy to enhance prediction accuracy effectively and utilizes symmetric trees as base learners to reduce the likelihood of overfitting. The validation accuracy of models built with the same independent variables using Stepwise Regression (SR) for LAI estimation is illustrated in Figure 10b. SR is a traditional statistical technique that automatically selects important variables from a large pool to build a predictive model. The results indicate that SR provides the best LAI estimation for FS, with an R^2 of 0.720 and an RPD of 1.736. However, the RPD for all three periods is below 2. CatBoost performs well across all three periods, with R^2 values greater than 0.8 and RPD values exceeding 2. SR's estimation accuracy is inferior to that of CatBoost. CatBoost excels in estimation accuracy, whether used with VIs alone or combined with texture information. Uribeetxebarria et al. [79] achieved precise wheat yield estimation with a spatial resolution of 10 m by combining satellite data with CatBoost, outperforming MLR, SVM, and RF. Similarly, Zhai et al. [80] integrated multi-source sensor data with soil–plant analysis development (SPAD) values and used the CatBoost algorithm to estimate the maize above-ground biomass, achieving higher accuracy than other models. However, CatBoost is currently not widely used in the inversion application of orchard LAI. It also demonstrates strong adaptability to small sample data, making it the most potent estimator in this study for apple orchard LAI estimation and inversion mapping.

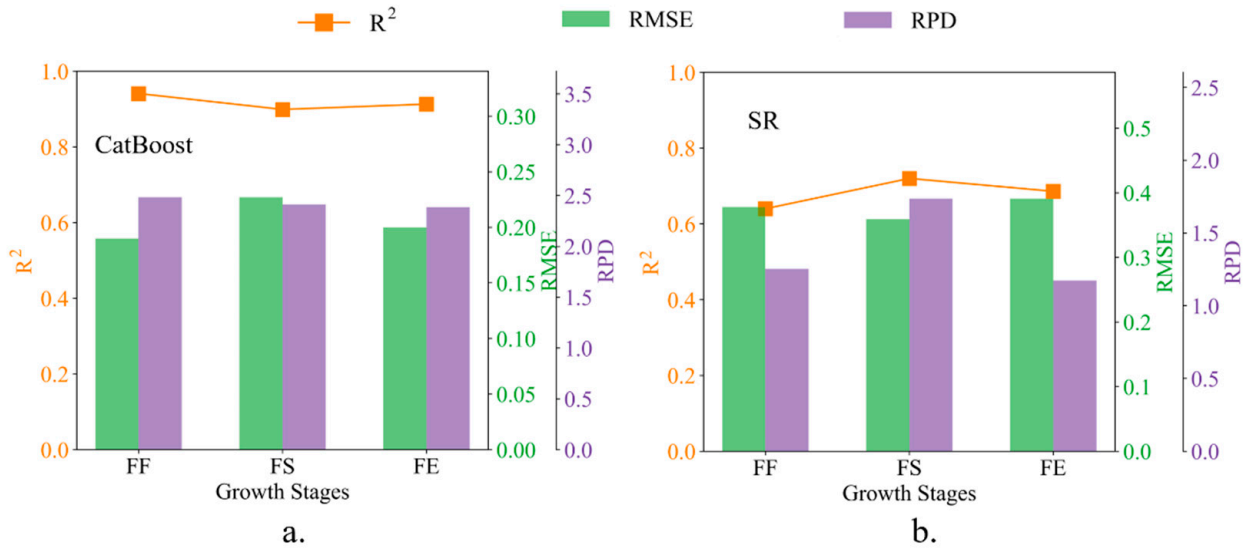

Figure 10. Validation accuracy of models constructed using VIs, TFs, and TIs as inputs. (**a**) CatBoost; (**b**) SR.

4.4. Advances and Limitation

While most precision agriculture focuses on staple crops such as winter wheat, rice, and corn, this study applies UAV multispectral technology to apples, an economically significant crop, to support rapid and non-destructive estimation of an apple orchard LAI. The LAI is crucial for plant photosynthesis and transpiration, making the rapid estimation of the canopy LAI essential for real-time monitoring of apple tree growth. When extracting texture features, Gabor transform stands out for its high sensitivity in capturing edge and texture information in images. It performs admirably in extracting the multispectral image texture features of apple orchards, an aspect that has been rarely explored in previous research. However, this study did not consider the use of physical models for estimating the apple orchard LAI, such as the PROSAIL model, which integrates the PROSPECT model for leaf optical properties and the SAIL model for canopy radiative transfer. Although the estimation accuracy of PROSAIL may be lower than that of VIs when sample sizes are sufficient, PROSAIL is capable of reflecting the physical processes of vegetation [30,81,82]. Collecting more physical data to construct physical models or integrating physical models with empirical approaches is necessary for future research, as this could potentially enhance the universality of LAI estimation.

5. Conclusions

This study extracted spectral and texture information from UAV multispectral images taken at different growth stages to construct VIs, TFs and TIs. The SVR-RFE algorithm was used for feature selection, and LAI estimation models were constructed for the respective growth stages, resulting in spatial distribution maps of the LAIs in apple orchards. The main conclusions are as follows: (1) Compared to using only spectral features, the inclusion of texture features extracted by Gabor transform across different growth stages significantly improved the accuracy of apple LAI estimation. The RPD for all models was greater than 2. (2) The LAI estimation models established using CatBoost exhibited high accuracy among the three models, with the FF showing the highest validation accuracy (validation set R^2 = 0.867, RMSE = 0.203, RPD = 2.482) and the best estimation capability across the three growth stages. (3) The combination of spectral and texture information from UAV multispectral images effectively estimated the apple orchard LAI. This approach can be used to monitor the growth and health of apple orchards in real-time, facilitating timely fertilization and irrigation. Consequently, it provides a scientific basis for orchard management, significantly reducing labor costs in agricultural practices.

Supplementary Materials: The supplementary materials of the complete ranking information can be downloaded at: https://www.mdpi.com/article/10.3390/rs16173237/s1.

Author Contributions: Conceptualization, J.Y. and Q.C.; methodology, J.Y.; software, J.Y. and Y.Z.; validation, J.Y. and Y.Z.; formal analysis, J.Y.; investigation, J.Y., Y.Z., Z.S., D.J., Y.G. and Y.L.; resources, Q.C.; data curation, J.Y.; writing—original draft preparation, J.Y.; writing—review and editing, J.Y.; visualization, J.Y.; supervision, Q.C.; project administration, Q.C.; funding acquisition, Q.C. All authors have read and agreed to the published version of the manuscript.

Funding: This research was funded by the National Natural Science Foundation of China (Grant Nos. 41701398 and 42071240).

Data Availability Statement: The original contributions presented in the study are included in the article, further inquiries can be directed to the corresponding author.

Acknowledgments: We would like to thank all the students in Chang's team for collecting the data for us.

Conflicts of Interest: The authors declare no conflict of interest.

Appendix A

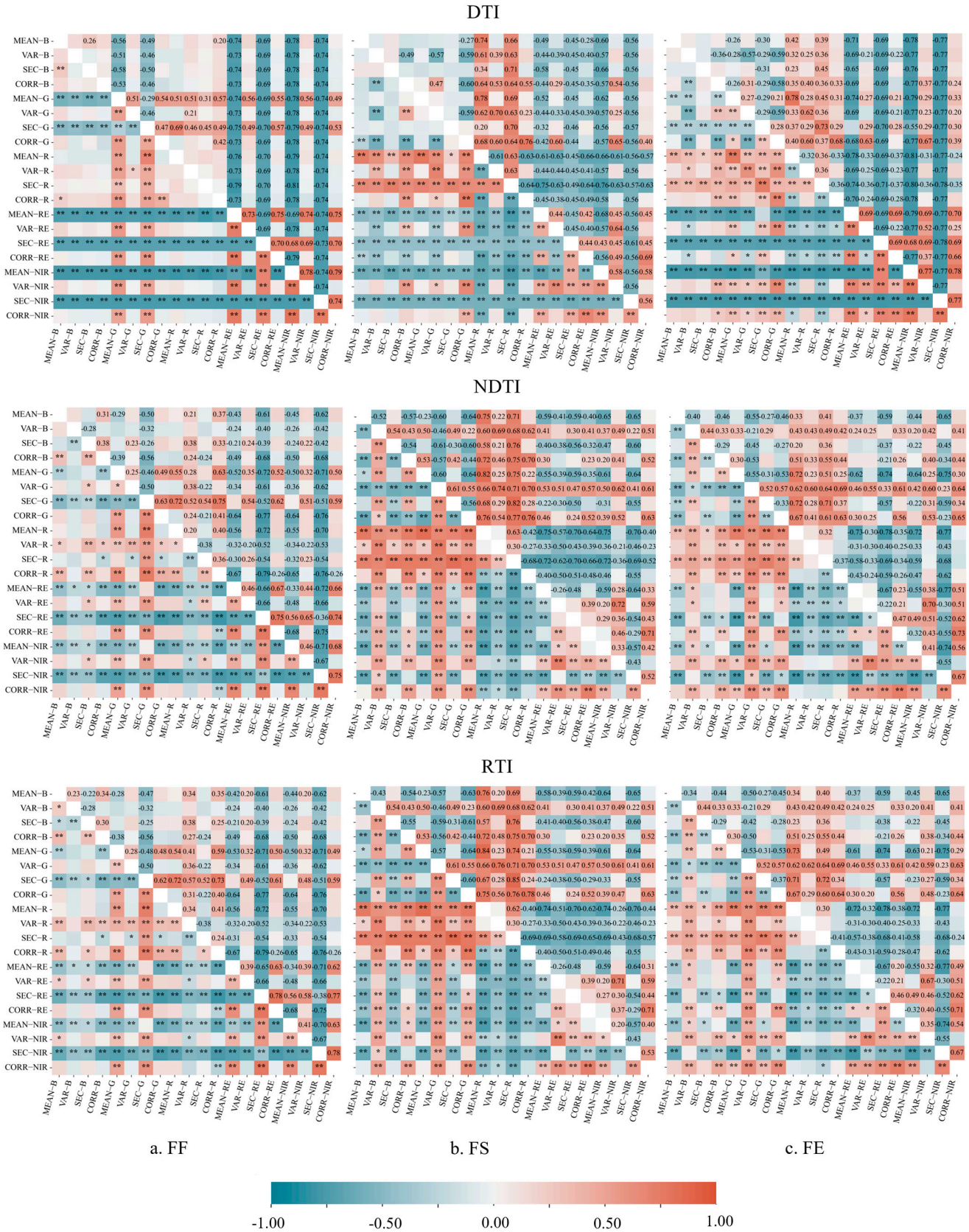

Figure A1. Correlation between TIs, composed of any two TFs, and LAI at different growth stages. * and ** indicate significant at the 0.05 and 0.01 levels, respectively.

References

1. Chen, M.; Shao, M.a.; Wei, X.; Li, T.; Shen, N.; Mi, M.; Zhao, C.; Yang, X.; Gan, M.; Bai, X. Response of the vertical distribution of soil water and nitrogen in the 5 m soil layer to the conversion of cropland to apple orchards in the Loess Plateau, China. *Agric. Ecosyst. Environ.* **2022**, *333*, 107960. [CrossRef]
2. Zhao, L.; Gao, X.; He, N.; Zhao, X. Ecohydrological advantage of young apple tree-based agroforestry and its response to extreme droughts on the semiarid Loess Plateau. *Agric. For. Meteorol.* **2022**, *321*, 108969. [CrossRef]
3. Zhu, Y.; Yang, G.; Yang, H.; Zhao, F.; Han, S.; Chen, R.; Zhang, C.; Yang, X.; Liu, M.; Cheng, J.; et al. Estimation of Apple Flowering Frost Loss for Fruit Yield Based on Gridded Meteorological and Remote Sensing Data in Luochuan, Shaanxi Province, China. *Remote Sens.* **2021**, *13*, 1630. [CrossRef]
4. Chen, J.M.; Black, T.A. Defining leaf area index for non-flat leaves. *Plant Cell Environ.* **2006**, *15*, 421–429. [CrossRef]
5. Nemani, R.; Pierce, L.; Running, S.; Band, L. Forest ecosystem processes at the watershed scale: Sensitivity to remotely-sensed Leaf Area Index estimates. *Int. J. Remote Sens.* **2007**, *14*, 2519–2534. [CrossRef]
6. Liu, C.; Kang, S.; Li, F.; Li, S.; Du, T. Canopy leaf area index for apple tree using hemispherical photography in arid region. *Sci. Hortic.* **2013**, *164*, 610–615. [CrossRef]
7. Macfarlane, C.; Grigg, A.; Evangelista, C. Estimating forest leaf area using cover and fullframe fisheye photography: Thinking inside the circle. *Agric. For. Meteorol.* **2007**, *146*, 1–12. [CrossRef]
8. Heenkenda, M.K.; Joyce, K.E.; Maier, S.W.; de Bruin, S. Quantifying mangrove chlorophyll from high spatial resolution imagery. *ISPRS J. Photogramm. Remote Sens.* **2015**, *108*, 234–244. [CrossRef]
9. Kamal, M.; Phinn, S.; Johansen, K. Assessment of multi-resolution image data for mangrove leaf area index mapping. *Remote Sens. Environ.* **2016**, *176*, 242–254. [CrossRef]
10. Qiao, L.; Zhao, R.; Tang, W.; An, L.; Sun, H.; Li, M.; Wang, N.; Liu, Y.; Liu, G. Estimating maize LAI by exploring deep features of vegetation index map from UAV multispectral images. *Field Crop. Res.* **2022**, *289*, 108739. [CrossRef]
11. Zhang, Y.; Ta, N.; Guo, S.; Chen, Q.; Zhao, L.; Li, F.; Chang, Q. Combining Spectral and Textural Information from UAV RGB Images for Leaf Area Index Monitoring in Kiwifruit Orchard. *Remote Sens.* **2022**, *14*, 1063. [CrossRef]
12. Lee, L.X.; Whitby, T.G.; Munger, J.W.; Stonebrook, S.J.; Friedl, M.A. Remote sensing of seasonal variation of LAI and fAPAR in a deciduous broadleaf forest. *Agric. For. Meteorol.* **2023**, *333*, 109389. [CrossRef]
13. Zhao, L.; Li, Q.; Chang, Q.; Shang, J.; Du, X.; Liu, J.; Dong, T. In-season crop type identification using optimal feature knowledge graph. *ISPRS J. Photogramm. Remote Sens.* **2022**, *194*, 250–266. [CrossRef]
14. Wang, K.; Franklin, S.E.; Guo, X.; Cattet, M. Remote sensing of ecology, biodiversity and conservation: A review from the perspective of remote sensing specialists. *Sensors* **2010**, *10*, 9647–9667. [CrossRef] [PubMed]
15. Gupta, S.K.; Pandey, A.C. Spectral aspects for monitoring forest health in extreme season using multispectral imagery. *Egypt. J. Remote Sens. Space Sci.* **2021**, *24*, 579–586. [CrossRef]
16. Imran, H.A.; Gianelle, D.; Rocchini, D.; Dalponte, M.; Martín, M.P.; Sakowska, K.; Wohlfahrt, G.; Vescovo, L. VIS-NIR, Red-Edge and NIR-Shoulder Based Normalized Vegetation Indices Response to Co-Varying Leaf and Canopy Structural Traits in Heterogeneous Grasslands. *Remote Sens.* **2020**, *12*, 2254. [CrossRef]
17. Liu, S.; Zeng, W.; Wu, L.; Lei, G.; Chen, H.; Gaiser, T.; Srivastava, A.K. Simulating the Leaf Area Index of Rice from Multispectral Images. *Remote Sens.* **2021**, *13*, 3663. [CrossRef]
18. Verrelst, J.; Rivera, J.P.; Veroustraete, F.; Muñoz-Marí, J.; Clevers, J.G.P.W.; Camps-Valls, G.; Moreno, J. Experimental Sentinel-2 LAI estimation using parametric, non-parametric and physical retrieval methods—A comparison. *ISPRS J. Photogramm. Remote Sens.* **2015**, *108*, 260–272. [CrossRef]
19. Zhao, D.; Zhen, J.; Zhang, Y.; Miao, J.; Shen, Z.; Jiang, X.; Wang, J.; Jiang, J.; Tang, Y.; Wu, G. Mapping mangrove leaf area index (LAI) by combining remote sensing images with PROSAIL-D and XGBoost methods. *Remote Sens. Ecol. Conserv.* **2023**, *9*, 370–389. [CrossRef]
20. Yi, Y.; Yang, D.; Huang, J.; Chen, D. Evaluation of MODIS surface reflectance products for wheat leaf area index (LAI) retrieval. *ISPRS J. Photogramm. Remote Sens.* **2008**, *63*, 661–677. [CrossRef]
21. Shen, B.; Ding, L.; Ma, L.; Li, Z.; Pulatov, A.; Kulenbekov, Z.; Chen, J.; Mambetova, S.; Hou, L.; Xu, D.; et al. Modeling the Leaf Area Index of Inner Mongolia Grassland Based on Machine Learning Regression Algorithms Incorporating Empirical Knowledge. *Remote Sens.* **2022**, *14*, 4196. [CrossRef]
22. Cortes, C.; Vapnik, V. Support-vector networks. *Mach. Learn.* **1995**, *20*, 273–297. [CrossRef]
23. Breiman, L. Random forests. *Mach. Learn.* **2001**, *45*, 5–32. [CrossRef]
24. Li, Q.; Wen, Z.; He, B. Practical Federated Gradient Boosting Decision Trees. *AAAI Conf. Artif. Intell.* **2020**, *34*, 4642–4649. [CrossRef]
25. Li, Z.-w.; Xin, X.-p.; Tang, H.; Yang, F.; Chen, B.-r.; Zhang, B.-h. Estimating grassland LAI using the Random Forests approach and Landsat imagery in the meadow steppe of Hulunber, China. *J. Integr. Agric.* **2017**, *16*, 286–297. [CrossRef]
26. Qiao, D.; Yang, J.; Bai, B.; Li, G.; Wang, J.; Li, Z.; Liu, J.; Liu, J. Non-Destructive Monitoring of Peanut Leaf Area Index by Combing UAV Spectral and Textural Characteristics. *Remote Sens.* **2024**, *16*, 2182. [CrossRef]

27. Liu, Y.; Zhang, Y.; Jiang, D.; Zhang, Z.; Chang, Q. Quantitative Assessment of Apple Mosaic Disease Severity Based on Hyperspectral Images and Chlorophyll Content. *Remote Sens.* **2023**, *15*, 2202. [CrossRef]
28. Zhang, Y.; Chang, Q.; Chen, Y.; Liu, Y.; Jiang, D.; Zhang, Z. Hyperspectral Estimation of Chlorophyll Content in Apple Tree Leaf Based on Feature Band Selection and the CatBoost Model. *Agronomy* **2023**, *13*, 2075. [CrossRef]
29. Liu, Z.; Guo, P.; Liu, H.; Fan, P.; Zeng, P.; Liu, X.; Feng, C.; Wang, W.; Yang, F. Gradient Boosting Estimation of the Leaf Area Index of Apple Orchards in UAV Remote Sensing. *Remote Sens.* **2021**, *13*, 3263. [CrossRef]
30. Zhang, C.; Chen, Z.; Yang, G.; Xu, B.; Feng, H.; Chen, R.; Qi, N.; Zhang, W.; Zhao, D.; Cheng, J.; et al. Removal of canopy shadows improved retrieval accuracy of individual apple tree crowns LAI and chlorophyll content using UAV multispectral imagery and PROSAIL model. *Comput. Electron. Agric.* **2024**, *221*, 108959. [CrossRef]
31. Du, X.; Zheng, L.; Zhu, J.; He, Y. Enhanced Leaf Area Index Estimation in Rice by Integrating UAV-Based Multi-Source Data. *Remote Sens.* **2024**, *16*, 1138. [CrossRef]
32. Wang, X.; Yan, S.; Wang, W.; Yin, L.; Li, M.; Yu, Z.; Chang, S.; Hou, F. Monitoring leaf area index of the sown mixture pasture through UAV multispectral image and texture characteristics. *Comput. Electron. Agric.* **2023**, *214*, 108333. [CrossRef]
33. Chen, S.; Useya, J.; Mugiyo, H. Decision-level fusion of Sentinel-1 SAR and Landsat 8 OLI texture features for crop discrimination and classification: Case of Masvingo, Zimbabwe. *Heliyon.* **2020**, *6*, e05358. [CrossRef]
34. Nogueira Martins, R.; de Assis de Carvalho Pinto, F.; Marçal de Queiroz, D.; Sárvio Magalhães Valente, D.; Tadeu Fim Rosas, J.; Fagundes Portes, M.; Sânzio Aguiar Cerqueira, E. Digital mapping of coffee ripeness using UAV-based multispectral imagery. *Comput. Electron. Agric.* **2023**, *204*, 107499. [CrossRef]
35. Du, R.; Lu, J.; Xiang, Y.; Zhang, F.; Chen, J.; Tang, Z.; Shi, H.; Wang, X.; Li, W. Estimation of winter canola growth parameter from UAV multi-angular spectral-texture information using stacking-based ensemble learning model. *Comput. Electron. Agric.* **2024**, *222*, 109074. [CrossRef]
36. Li, W.; Wang, J.; Zhang, Y.; Yin, Q.; Wang, W.; Zhou, G.; Huo, Z. Combining Texture, Color, and Vegetation Index from Unmanned Aerial Vehicle Multispectral Images to Estimate Winter Wheat Leaf Area Index during the Vegetative Growth Stage. *Remote Sens.* **2023**, *15*, 5715. [CrossRef]
37. Qi, K.-T.; Zhang, H.-S.; Zheng, Y.-G.; Zhang, Y.; Ding, L.-Y. Stripe segmentation of oceanic internal waves in SAR images based on Gabor transform and K-means clustering. *Oceanologia* **2023**, *65*, 548–555. [CrossRef]
38. Grigorescu, S.E.; Petkov, N.; Kruizinga, P. Comparison of texture features based on Gabor filters. *IEEE Trans. Image Process.* **2002**, *11*, 1160–1167. [CrossRef]
39. Zhang, D.; Wong, A.; Indrawan, M.; Lu, G. Content-based image retrieval using Gabor texture features. *IEEE Trans. Pattern Anal. Mach. Intell.* **2000**, *3656*, 13–15.
40. Daugman, J.G. Complete discrete 2-D Gabor transforms by neural networks for image analysis and compression. *IEEE Trans. Acoust. Speech Signal Process.* **1988**, *36*, 1169–1179. [CrossRef]
41. Liu, S.; Jin, X.; Bai, Y.; Wu, W.; Cui, N.; Cheng, M.; Liu, Y.; Meng, L.; Jia, X.; Nie, C.; et al. UAV multispectral images for accurate estimation of the maize LAI considering the effect of soil background. *Int. J. Appl. Earth Obs. Geoinf.* **2023**, *121*, 103383. [CrossRef]
42. Yuan, W.; Meng, Y.; Li, Y.; Ji, Z.; Kong, Q.; Gao, R.; Su, Z. Research on rice leaf area index estimation based on fusion of texture and spectral information. *Comput. Electron. Agric.* **2023**, *211*, 108016. [CrossRef]
43. Zhang, B.; Gu, L.; Dai, M.; Bao, X.; Sun, Q.; Zhang, M.; Qu, X.; Li, Z.; Zhen, W.; Gu, X. Estimation of grain filling rate of winter wheat using leaf chlorophyll and LAI extracted from UAV images. *Field Crops Res.* **2024**, *306*, 109198. [CrossRef]
44. Ta, N.; Chang, Q.; Zhang, Y. Estimation of Apple Tree Leaf Chlorophyll Content Based on Machine Learning Methods. *Remote Sens.* **2021**, *13*, 3902. [CrossRef]
45. Li, W.; Yuan, Y.; Hu, S.; Li, M.; Feng, W.; Zheng, J.; Lv, J. Positioning of Apple's Growth Cycle Based on Pattern Recognition. *Mob. Inf. Syst.* **2021**, 9687950. [CrossRef]
46. Rouse, J.W.; Haas, R.H.; Schell, J.A.; Deering, D.W. Monitoring vegetation systems in the Great Plains with ERTS. *NASA Spec. Publ.* **1974**, *351*, 309.
47. Tucker, C.J. Red and photographic infrared linear combinations for monitoring vegetation. *Remote Sens. Environ.* **1979**, *8*, 127–150. [CrossRef]
48. Richardson, A.J.; Wiegand, C.L. Distinguishing vegetation from soil background information. *Photogramm. Eng. Remote Sens.* **1977**, *43*, 1541–1552.
49. Zhou, X.; Dandan, L.; Huiming, Y.; Honggen, C.; Leping, S.; Guojing, Y.; Qingbiao, H.; Brown, L.; Malone, J.B. Use of landsat TM satellite surveillance data to measure the impact of the 1998 flood on snail intermediate host dispersal in the lower Yangtze River Basin. *Acta Trop.* **2002**, *82*, 199–205. [CrossRef]
50. Roujean, J.-L.; Breon, F.-M. Estimating PAR absorbed by vegetation from bidirectional reflectance measurements. *Remote Sens. Environ.* **1995**, *51*, 375–384. [CrossRef]
51. Hunt, E.R.; Cavigelli, M.; Daughtry, C.S.T.; McMurtrey, J.E.; Walthall, C.L. Evaluation of digital photography from model aircraft for remote sensing of crop biomass and nitrogen status. *Precis. Agric.* **2005**, *6*, 359–378. [CrossRef]
52. Sripada, R.P.; Heiniger, R.W.; White, J.G.; Meijer, A.D. Aerial color infrared photography for determining early in-season nitrogen requirements in corn. *Agron. J.* **2006**, *98*, 968–977. [CrossRef]

53. Buschmann, C.; Nagel, E. In vivo spectroscopy and internal optics of leaves as basis for remote sensing of vegetation. *Int. J. Remote Sens.* **1993**, *14*, 711–722. [CrossRef]
54. Gao, X.; Huete, A.R.; Ni, W.; Miura, T. Optical–biophysical relationships of vegetation spectra without background contamination. *Remote Sens. Environ.* **2000**, *74*, 609–620. [CrossRef]
55. Rondeaux, G.; Steven, M.; Baret, F. Optimization of soil-adjusted vegetation indices. *Remote Sens. Environ.* **1996**, *55*, 95–107. [CrossRef]
56. Dash, J.; Curran, P.J. The MERIS terrestrial chlorophyll index. *Int. J. Remote Sens.* **2004**, *25*, 5403–5413. [CrossRef]
57. Gitelson, A.A.; Gritz, Y.; Merzlyak, M.N. Relationships between leaf chlorophyll content and spectral reflectance and algorithms for non-destructive chlorophyll assessment in higher plant leaves. *J. Plant Physiol.* **2003**, *160*, 271–282. [CrossRef] [PubMed]
58. Jiang, Z.; Huete, A.R.; Didan, K.; Miura, T. Development of a two-band enhanced vegetation index without a blue band. *Remote Sens. Environ.* **2008**, *112*, 3833–3845. [CrossRef]
59. Gitelson, A.A.; Merzlyak, M.N. Remote sensing of chlorophyll concentration in higher plant leaves. *Adv. Space Res.* **1998**, *22*, 689–692. [CrossRef]
60. Broge, N.H.; Leblanc, E. Comparing prediction power and stability of broadband and hyperspectral vegetation indices for estimation of green leaf area index and canopy chlorophyll density. *Remote Sens. Environ.* **2001**, *76*, 156–172. [CrossRef]
61. Schneider, P.; Roberts, D.A.; Kyriakidis, P.C. A VARI-based relative greenness from MODIS data for computing the Fire Potential Index. *Remote Sens. Environ.* **2008**, *112*, 1151–1167. [CrossRef]
62. Huete, A.R. A soil-adjusted vegetation index (SAVI). *Remote Sens. Environ.* **1988**, *25*, 295–309. [CrossRef]
63. Haboudane, D.; Miller, J.R.; Pattey, E.; Zarco-Tejada, P.J.; Strachan, I.B. Hyperspectral vegetation indices and novel algorithms for predicting green LAI of crop canopies: Modeling and validation in the context of precision agriculture. *Remote Sens. Environ.* **2004**, *90*, 337–352. [CrossRef]
64. Peñuelas, J.; Filella, I.; Gamon, J.A. Assessment of photosynthetic radiation-use efficiency with spectral reflectance. *New Phytol.* **1995**, *131*, 291–296. [CrossRef]
65. Turner, M.R. Texture discrimination by Gabor functions. *Biol. Cybern.* **1986**, *55*, 71–82. [CrossRef]
66. Jiang, B.; Wang, P.; Zhuang, S.; Li, M.; Li, Z.; Gong, Z. Detection of maize drought based on texture and morphological features. *Comput. Electron. Agric.* **2018**, *151*, 50–60. [CrossRef]
67. Zheng, H.; Cheng, T.; Zhou, M.; Li, D.; Yao, X.; Tian, Y.; Cao, W.; Zhu, Y. Improved estimation of rice aboveground biomass combining textural and spectral analysis of UAV imagery. *Precis. Agric.* **2019**, *20*, 611–629. [CrossRef]
68. Feng, L.; Zhang, Z.; Ma, Y.; Du, Q.; Williams, P.; Drewry, J.; Luck, B. Alfalfa Yield Prediction Using UAV-Based Hyperspectral Imagery and Ensemble Learning. *Remote Sens.* **2020**, *12*, 2028. [CrossRef]
69. Wu, L.; Huang, G.; Fan, J.; Zhang, F.; Wang, X.; Zeng, W. Potential of kernel-based nonlinear extension of Arps decline model and gradient boosting with categorical features support for predicting daily global solar radiation in humid regions. *Energy Convers. Manag.* **2019**, *183*, 280–295. [CrossRef]
70. Mutanga, O.; Adam, E.; Cho, M.A. High density biomass estimation for wetland vegetation using WorldView-2 imagery and random forest regression algorithm. *Int. J. Appl. Earth Obs. Geoinf.* **2012**, *18*, 399–406. [CrossRef]
71. Shah, S.H.; Angel, Y.; Houborg, R.; Ali, S.; McCabe, M.F. A random forest machine learning approach for the retrieval of leaf chlorophyll content in wheat. *Remote Sens.* **2019**, *11*, 920. [CrossRef]
72. Cui, Y.; Meng, F.; Fu, P.; Yang, X.; Zhang, Y.; Liu, P. Application of hyperspectral analysis of chlorophyll a concentration inversion in Nansi Lake. *Ecol. Inform.* **2021**, *64*, 101360. [CrossRef]
73. Ge, Y.; Bai, G.; Stoerger, V.; Schnable, J.C. Temporal dynamics of maize plant growth, water use, and leaf water content using automated high throughput RGB and hyperspectral imaging. *Comput. Electron. Agric.* **2016**, *127*, 625–632. [CrossRef]
74. Sun, X.; Yang, Z.; Su, P.; Wei, K.; Wang, Z.; Yang, C.; Wang, C.; Qin, M.; Xiao, L.; Yang, W.; et al. Non-destructive monitoring of maize LAI by fusing UAV spectral and textural features. *Front. Plant Sci.* **2023**, *14*, 1158837. [CrossRef]
75. Zou, M.; Liu, Y.; Fu, M.; Li, C.; Zhou, Z.; Meng, H.; Xing, E.; Ren, Y. Combining spectral and texture feature of UAV image with plant height to improve LAI estimation of winter wheat at jointing stage. *Front. Plant Sci.* **2024**, *14*, 1272049. [CrossRef]
76. Hang, Y.; Su, H.; Yu, Z.; Liu, H.; Guan, H.; Kong, F. Estimation of rice leaf area index combining UAV spectrum, texture features and vegetation coverage. *Trans. Chin. Soc. Agric. Eng.* **2021**, *37*, 64–71.
77. Zhang, J.; Qiu, X.; Wu, Y.; Zhu, Y.; Cao, Q.; Liu, X.; Cao, W. Combining texture, color, and vegetation indices from fixed-wing UAS imagery to estimate wheat growth parameters using multivariate regression methods. *Comput. Electron. Agric.* **2021**, *185*, 106138. [CrossRef]
78. Fei, S.; Hassan, M.A.; Xiao, Y.; Su, X.; Chen, Z.; Cheng, Q.; Duan, F.; Chen, R.; Ma, Y. UAV-based multi-sensor data fusion and machine learning algorithm for yield prediction in wheat. *Precision Agric.* **2023**, *24*, 187–212. [CrossRef] [PubMed]
79. Uribeetxebarria, A.; Castellón, A.; Aizpurua, A. Optimizing Wheat Yield Prediction Integrating Data from Sentinel-1 and Sentinel-2 with CatBoost Algorithm. *Remote Sens.* **2023**, *15*, 1640. [CrossRef]
80. Zhai, W.; Li, C.; Fei, S.; Liu, Y.; Ding, F.; Cheng, Q.; Chen, Z. CatBoost algorithm for estimating maize above-ground biomass using unmanned aerial vehicle-based multi-source sensor data and SPAD values. *Comput. Electron. Agric.* **2023**, *214*, 108306. [CrossRef]

81. Li, D.; Chen, J.M.; Yu, W.; Zheng, H.; Yao, X.; Zhu, Y.; Cao, W.; Cheng, T. A chlorophyll-constrained semi-empirical model for estimating leaf area index using a red-edge vegetation index. *Comput. Electron. Agric.* **2024**, *220*, 108891. [CrossRef]
82. Jay, S.; Maupas, F.; Bendoula, R.; Gorretta, N. Retrieving LAI, chlorophyll and nitrogen contents in sugar beet crops from multi-angular optical remote sensing: Comparison of vegetation indices and PROSAIL inversion for field phenotyping. *Field Crops Res.* **2017**, *210*, 33–46. [CrossRef]